The Astrophysical Journal, 877:114 (17pp), 2019 June 1 https://doi.org/10.3847/1538-4357/ab12d1

TRAO Survey of Nearby Filamentary Molecular Clouds, the Universal Nursery of Stars (TRAO FUNS). I. Dynamics and Chemistry of L1478 in the California Molecular Cloud

Eun Jung Chung[1], Chang Won Lee[1,9], Shinyoung Kim[1,9], Gwanjeong Kim[2], Paola Caselli[3], Mario Tafalla[4], Philip C. Myers[5], Archana Soam[6], Tie Liu[1], Maheswar Gopinathan[7], Miryang Kim[1], Kyoung Hee Kim[1,8], Woojin Kwon[1,9], Hyunwoo Kang[1], and Changhoon Lee[1]

[1] Korea Astronomy and Space Science Institute, 776 Daedeokdae-ro, Yuseong-gu, Daejeon 34055, Republic of Korea
[2] Nobeyama Radio Observatory, National Astronomical Observatory of Japan, National Institutes of Natural Sciences, Nobeyama, Minamimaki, Minamisaku, Nagano 384-1305, Japan
[3] Max-Planck-Institut für Extraterrestrische Physik, D-85748 Garching, Germany
[4] Observatorio Astronómico Nacional (IGN), Alfonso XII 3, E-28014 Madrid, Spain
[5] Harvard-Smithsonian Center for Astrophysics, 60 Garden Street, Cambridge, MA 02138, USA
[6] SOFIA Science Center, USRA, NASA Ames Research Center, MS-12 N232, Moffett Field, CA 94035, USA
[7] Indian Institute of Astrophysics, Koramangala, Bangalore 560034, India
[8] Department of Earth Science Education, Kongju National University, 56 Gongjudaehak-ro, Gongju-si, Chungcheongnam-do 32588, Republic of Korea
[9] University of Science and Technology, Korea (UST), 217, Gajeong-ro, Yuseong-gu, Daejeon, 34113, Republic of Korea
Received 2018 July 15; revised 2019 March 3; accepted 2019 March 22; published 2019 May 31

Abstract

"TRAO FUNS" is a project to survey the Gould Belt's clouds in molecular lines. This paper presents its first results on the central region of the California molecular cloud, L1478. We performed on-the-fly mapping observations using the Taeduk Radio Astronomy Observatory 14 m single-dish telescope equipped with a 16 multibeam array covering a ∼1.0 square degree area of this region using $C^{18}O(1–0)$, mainly tracing low-density clouds, and a ∼460 square arcminute area using $N_2H^+(1–0)$, mainly tracing dense cores. CS(2–1) and $SO(3_2–2_1)$ were also used simultaneously to map a ∼440 square arcminute area of this region. We identified 10 filaments by applying the dendrogram technique to the $C^{18}O$ data cube and 8 dense N_2H^+ cores using FELLWALKER. Basic physical properties of filaments such as mass, length, width, velocity field, and velocity dispersion are derived. It is found that L1478 consists of several filaments with slightly different velocities. Particularly, the filaments that are supercritical are found to contain dense cores detected in N_2H^+. A comparison of nonthermal velocity dispersions derived from $C^{18}O$ and N_2H^+ for the filaments and dense cores indicates that some of the dense cores share kinematics similar to those of the surrounding filaments, while several dense cores have different kinematics from those of their filaments. This suggests that the formation mechanism of dense cores and filaments can be different in individual filaments depending on their morphologies and environments.

Key words: ISM: clouds – ISM: kinematics and dynamics – ISM: structure – stars: formation

1. Introduction

How stars form in molecular clouds is one of the key questions in astronomy. In general, stars are known to form by a gravitational contraction in dense cores, which are made in less dense molecular clouds by their hierarchical fragmentation. Recent high-resolution observations mainly done by the *Spitzer Space Telescope*[10] and *Herschel Space Observatory*[11] reveal that molecular clouds are filamentary, and such a structure is ubiquitous over various star-forming environments, from active star-forming molecular clouds like the Orion molecular complex to non-star-forming molecular clouds such as the Polaris flare (e.g., André et al. 2010; Hacar et al. 2018).

During the last decade, several studies have been done and progress has been made in understanding the physical properties of filaments and dense cores. One of the most interesting findings about filaments is that filaments have a characteristic width of 0.1 pc, which is comparable to the typical size of dense cores (e.g., André et al. 2010; Arzoumanian et al. 2011, 2019; Palmeirim et al. 2013; Federrath 2016). Most prestellar cores are found on the dense, supercritical filaments where the mass per unit length is larger than the critical value of isothermal cylinders (e.g., André et al. 2010; Könyves et al. 2015; Marsh et al. 2016). Many young stellar groups in the nearby molecular clouds are found to be well associated with a hub–filament structure that consists of a hub that is a central body with relatively higher column density ($>10^{22}$ cm^{-2}) and filaments radiating from the hub that have lower column density (e.g., Myers 2009, and references therein). In addition, velocity gradients have been observed along filaments, and the gas flow along filaments is responsible for the formation of the star cluster (e.g., Kirk et al. 2013; Peretto et al. 2014; Imara et al. 2017; Baug et al. 2018; Yuan et al. 2018). Hence, it seems clear that filaments can play a crucial role in the formation of cores and stars.

These results raise important questions, such as (1) how do filaments and dense cores form in large molecular clouds?, and (2) are filaments an intermediate stage of star formation, that is, from large clouds to dense cores? These can be answered by probing the kinematics and chemistry of filaments and dense cores with systematic molecular line observations toward various molecular clouds.

We have been performing such observations for filament clouds using the Taeduk Radio Astronomy Observatory (TRAO)[12] 14 m antenna with the project "TRAO FUNS," which is an acronym for "the TRAO survey of Filaments, the Universal Nursery of Stars." The project is to make a systematic survey of 10 Gould Belt clouds with several molecular lines in various

[10] https://www.cfa.harvard.edu/gouldbelt/
[11] http://www.herschel.fr/cea/gouldbelt/en/
[12] http://radio.kasi.re.kr/trao/main_trao.php

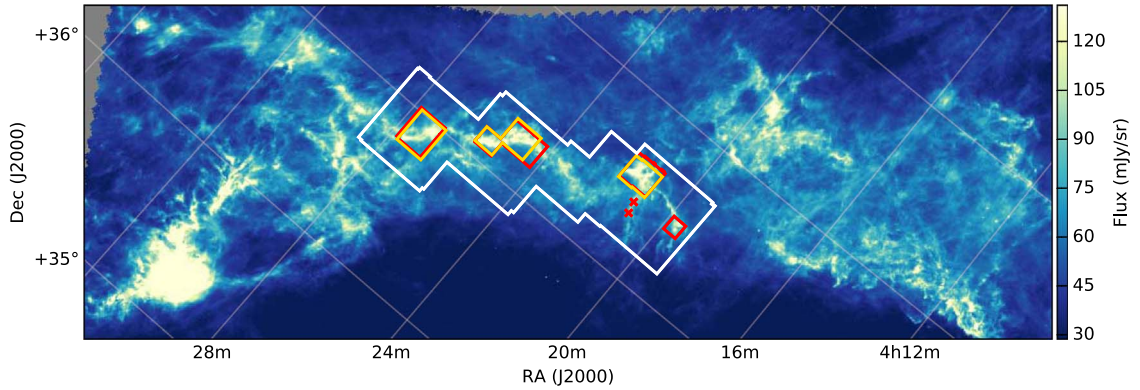

Figure 1. *Herschel* 250 μm image of the Auriga-California region. The area covered in this study, L1478, is indicated by white (^{13}CO and C^{18}O 1–0), red (N_2H^+ and HCO^+ 1–0), and yellow (SO 3_2–2_1 and CS 2–1) boxes. The red crosses show the region where position-switching mode observations of N_2H^+ and HCO^+ molecular lines have been done.

environments, aiming to obtain (1) the velocity structure of filaments and dense cores for the study of their formation, (2) radial accretion or inward motions toward dense cores from their surrounding filaments, and (3) chemical differentiation of filaments and their dense cores. For these goals, six molecular lines, C^{18}O (1–0), ^{13}CO (1–0), N_2H^+ (1–0), HCO^+ (1–0), SO (3_2–2_1), and CS (2–1), are selected as tracers of the kinematics and chemical evolution of the filaments and dense cores. More details on TRAO FUNS will be introduced in another paper by C. W. Lee et al. (2019, in preparation).

In this paper, we present the first results of the TRAO FUNS toward L1478 in the California molecular cloud (CMC). The CMC, which is also called the Auriga-California molecular cloud, has been recently recognized as a massive giant molecular cloud by Lada et al. (2009). They used an infrared extinction map from the Two Micron All Sky Survey (Kleinmann et al. 1994) and CO maps from the Galactic plane survey (Dame et al. 2001) and found a continuous distribution of the molecular cloud in velocity and space as a single molecular cloud at the same distance. CMC is located at a distance of 450 ± 23 pc, and it is comparable in size ($\sim$80 pc) and mass ($\sim 10^5\ M_\odot$) to the Orion giant molecular cloud (OMC). However, the number of young stellar objects (YSOs) in CMC (149) is 15–20 times smaller than that of OMC (3330; Broekhoven-Fiene et al. 2014). Harvey et al. (2013) investigated the YSOs and dense gas of CMC, finding 60 compact sources at 70/160 μm and 11 cold, compact sources at 1.1 mm. Recently, Broekhoven-Fiene et al. (2018) identified 59 candidate protostars and found that 24 among them are associated with YSOs in the catalogs of *Spitzer* and *Herschel*/PACS. They suggested that CMC is significantly less efficient in star formation than Orion A. There are recent observations of molecular lines for a part of CMC by Imara et al. (2017). They investigated the relationship of filaments and dense cores in the CMC region ($\sim 0.^\circ 5 \times 0.^\circ 5$ area) with dust continuum data (*Herschel*) and ^{12}CO and ^{13}CO (2–1) molecular line data obtained from the Heinrich Hertz Submillimeter Telescope, finding that filaments in the west region of L1478 are velocity-coherent and gravitationally supercritical.

We have investigated filaments and dense cores of CMC region L1478 ($\sim 2^\circ \times 0.^\circ 5$), which provides a good laboratory to investigate the formation of filaments and dense cores. Various morphologies of filaments such as a long network of filaments and a hub–filament structure can be found (see Figure 1). Also, the star-forming property of L1478 is relatively modest and it seems to be a low-mass star-forming region, in the sense that only three YSOs are found, and thus it can be a good comparison to the OMC (Broekhoven-Fiene et al. 2018). Our survey provides the first mapping observations in various molecule lines toward the central region of the CMC.

This paper is organized as follows. In Section 2, observation and data reduction are explained. Identifications of filaments and dense cores and their basic physical properties are presented in Section 3. In Section 4, we discuss the velocity structure of filaments, gravitational instability, and the formation mechanisms of filaments and dense cores. Section 5 summarizes our results.

2. Observations and Data Reduction

2.1. Observations

We have carried out on-the-fly (OTF) mapping observations toward L1478 in CMC with the TRAO 14 m telescope from 2017 January to May and from 2017 December to 2018 February. The equipped front end is SEcond QUabbin Optical Image Array (SEQUOIA-TRAO), which consists of a 4×4 array receiver, and its spatial separation is 89″. The back-end fast Fourier transform spectrometer has 4096×2 channels at 15 kHz resolution ($\sim$0.04 km s^{-1} at 110 GHz), which covers a total bandwidth of 62.5 MHz, corresponding to $\sim$170 km s^{-1} at 110 GHz. TRAO systems allow simultaneous observations of two molecular lines in the frequency ranges of 85 and 100 GHz or 100 and 115 GHz. The beam efficiency at 90 GHz is 0.48, and at 110 GHz it is 0.46.

To investigate the physical properties of filaments and dense cores, six molecular lines are observed. C^{18}O and N_2H^+(1–0) molecular lines are chosen as a tracer of relatively less dense material for the filaments and a dense gas tracer for dense cores, respectively. ^{13}CO(1–0), which can reveal the large-scale bulk motion, is simultaneously obtained with C^{18}O. With N_2H^+ observation, HCO^+(1–0) is concurrently observed. To probe the chemical evolution of dense cores, SO(3_2–2_1) is selected, and CS(2–1) is observed at the same time. SO(3_2-2_1) is known as one of the most sensitive molecules to depletion and hence can be used as a tracer of very young dense cores (Tafalla et al. 2006). The CS(2–1) line was chosen to be useful to study infall motions in the prestellar cores (Lee et al. 2001). In this study,

Table 1
Observations

Molecule	ν_{ref}[a] (GHz)	θ_{FWHM}[b] ($''$)	Area[c] (sq. arcmin)	θ_{pixel}[d] ($''$)	δv[d] (km s^{-1})	rms[e] (K[T_A^*])
$C^{18}O$ (1–0)	109.782160	47	~3700	44	0.1	0.092
^{13}CO (1–0)	110.201353	47	~3700	44	0.1	0.097
N_2H^+ (1–0)	93.173764	56	~460	22	0.06	0.063
HCO^+ (1–0)	89.188525	58	~460	22	0.06	0.062
SO (3_2–2_1)	99.299870	52	~440	22	0.06	0.094
CS (2–1)	97.980953	52	~440	22	0.06	0.097

Notes.
[a] Rest frequency of each molecular line is taken from the Cologne Database for Molecular Spectroscopy (CDMS; Müller et al. 2001, https://cdms.ph1.uni-koeln.de/cdms/portal/).
[b] FWHM of the beam.
[c] Total observed area.
[d] The pixel size and channel width of the final data cube.
[e] Noise level in T_A^* of the final data cube.

four molecular lines $C^{18}O$, N_2H^+, CS, and SO are mainly used in the analyses.

We divided our target area of $C^{18}O$ (and ^{13}CO simultaneously) into five regions that have a box shape, referred to as "tiles" hereafter, shown in Figure 1, and we carried out OTF mapping observations. Each tile has a size from $12' \times 12'$ to $32' \times 32'$. The scanning rate was $55''$ per second and the integration time is 0.2 s. A scan step of 0.25 half-power beam width (HPBW; $44''$) along the scan direction and 0.75 HPBW separation between the rows are applied for $C^{18}O$ and ^{13}CO. We carried out OTF mapping observations of N_2H^+ and HCO^+ toward the regions only where $C^{18}O$ is strongly detected. Five tiles were observed with a scan step of 0.25 HPBW ($44''$) along the scan direction and a 0.25 HPBW separation between the rows. Simultaneous observations of SO and CS lines are performed with the same OTF mapping parameters as the observations of $C^{18}O$ and ^{13}CO, but for only four tiles. We made maps alternatively along the R.A. and decl. directions. In Figure 1, the observed areas of the six molecular lines are presented with the *Herschel* 250 μm continuum image. Toward two points where $C^{18}O$ is strongly detected but OTF observation of N_2H^+ and HCO^+ was not carried out, additional position-switching (PS) observations of N_2H^+ (and HCO^+) have been carried out because of the lack of observing time (denoted with red crosses in Figure 1). The rms noise level of PS observations is about 0.06 K in the unit of antenna temperature for both lines.

2.2. Data Reduction

The raw OTF data for each map of each tile are read and turned into a map with a jinc-Gaussian function after baseline fitting (with first order) in OTFTOOL. We give the resulting cell size of $22''$ and apply noise-weighting. Further reductions and examinations are done with the CLASS[13] package. Since the baseline is not good in either end of the band and the total velocity range of the spectra (~170 km s^{-1}) is much larger than that of emissions in our object (less than 20 km s^{-1}), baseline fittings are done in two steps. First, both ends of the spectra were cut off so that the velocity range becomes 120 km s^{-1}, and a baseline was subtracted with the second-order polynomial. After that, the spectra are resampled with a channel width of 0.06 km s^{-1}, and both ends were cut off again, resulting in a spectral velocity range of 60 km s^{-1}, and baseline subtraction was done again with a first-order polynomial. After this step, all channel maps are examined, and maps having a high noise level or showing some spatial gradient of noise level due to the change in system temperature were excluded. Finally, the maps are merged into a final fits cube with $44''$ cell size and 0.1 km s^{-1} velocity channel width for $C^{18}O$ and ^{13}CO, and $22''$ cell size and 0.06 km s^{-1} velocity channel width for the other molecular lines. The basic observational information is given in Table 1.

3. Filaments and Dense Cores

3.1. Filament Identification

Figure 2 shows the integrated intensity maps of ^{13}CO (top) and $C^{18}O$ (bottom) on a *Herschel* 250 μm image. The distributions of molecules seem to well match that of the dust continuum. The long filamentary structure from the southeast to the center of the observed area is well revealed by $C^{18}O$ as well as ^{13}CO. It spreads out to ~1° in the sky. The other noticeable feature is the hub–filament structure in the northwest that is referred to as Cal-X because of its X shape by Imara et al. (2017). The hub radiates four filaments to the east, south, west, and north.

^{13}CO is detected at the outer edge of the observed regions, while $C^{18}O$ is well matched to the filamentary dust emission. Most of the ^{13}CO spectra show multiple velocity components. In the top panel, ^{13}CO emission is detected at ~1 km s^{-1} and ~−1.5 km s^{-1}, while $C^{18}O$ is only detected at ~−1.5 km s^{-1} with a single Gaussian shape, indicating that the double-peak component at ~−1.5 km s^{-1} of ^{13}CO is a self-absorption feature. Therefore, ^{13}CO spectra are thought to be self-absorbed toward some dense regions shown in the spectra (a) to (d), because they have a relatively larger optical depth than that of $C^{18}O$. However, both ^{13}CO and $C^{18}O$ spectra at several positions drawn in the bottom panel of Figure 2 show double-peaked features, implying that the filaments at these places may consist of multiple components to the line of sight.

To identify filaments with a multiple velocity structure, we used the astrodendro[14] Python package and applied it to the $C^{18}O$ data cube. A dendrogram is a tree diagram that shows

[13] http://www.iram.fr/IRAMFR/GILDAS

[14] https://dendrograms.readthedocs.io

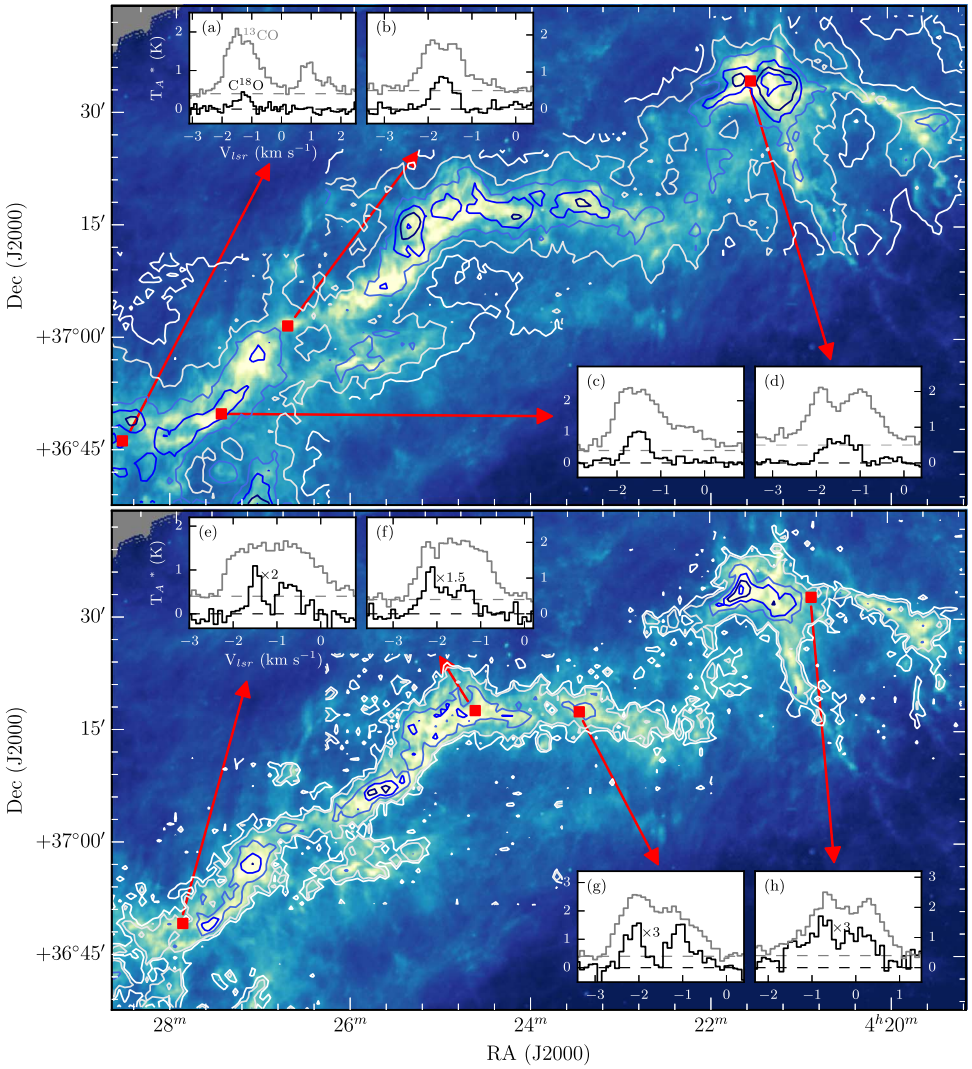

Figure 2. Integrated intensity maps of ^{13}CO(1–0) (top) and C^{18}O(1–0) (bottom) toward L1478. Background color images are *Herschel* 250 μm data, and the CO intensity maps are shown in contours. The line intensity maps are integrated over a velocity range of −3.8 to 2.3 km s^{-1} for ^{13}CO, and −3.2 to 0.6 km s^{-1} for C^{18}O. The contour levels of ^{13}CO are $7n \times \sigma_{\rm rms}$ (n = 1, 2, ⋯, 6) and those of C^{18}O are 2 and $3n \times \sigma_{\rm rms}$ (n = 1, 2, ⋯, 6). Two spectra of ^{13}CO (gray) and C^{18}O (black) are given in (a)–(h) inset windows at the selected positions. The spectra in windows (a)–(d) are given to illustrate that C^{18}O traces well the velocity field of filament material, while ^{13}CO is more or less self-absorbed due to its larger optical depth compared with C^{18}O. The spectra in (e)–(h) are shown to indicate that C^{18}O profiles have two components, and thus some of the filaments can have a multiple velocity structure to the line of sight.

how and where the structures merge, and its algorithm identifies the hierarchical structure of two- and three-dimensional data sets. Structures start from local maxima, their volumes get bigger, merging with the surroundings with lower flux densities, and stop when they meet neighboring structures (Rosolowsky et al. 2008). Details of filament identification using the dendrogram technique are given in the Appendix.

Figure 3 shows the results of this dendrogram analysis. Resulting branches and leaves are shown in the dendrogram tree (top), and its spatial distribution in the filament clouds is presented in the bottom panel on the C^{18}O moment 0 image. Each identified leaf is indicated with a color-coded base on their numbers, with the same color in the tree and map. Five false leaves are found that are due to noisy observation near the boundary of the map. We excluded them and used the other 10 filaments in the analysis. With the given mask in the dendrogram, we extract data cubes of each filament and use them for further analyses, that is, for central velocity and velocity dispersion. It is noticeable here that F6 (filament 6), F7, and F8 are identified as independent leaves, but they have a single stem, and this is the same for filaments from F1 to F5. Only F9 and F10 have their own stems. We will discuss these filaments later.

3.2. Dense Core Identification

The N_2H^+(1–0) molecular line, which is usually optically thin, is an appropriate tracer of dense cores in nearby star-forming regions (e.g., Caselli et al. 1995; Sanhueza et al. 2012). To probe the relationship of dense cores and filaments, we made five OTF tiles of N_2H^+ toward the regions where C^{18}O emission is strongly detected. Two tiles are in F4, one in F5, one in F6, and one in F8 (see Figures 1 and 3). N_2H^+ emission is detected in all of the observed tiles except in F6. We also carried out PS observations toward two positions in F7 (marked with red crosses in Figure 1), but N_2H^+ was not detected at the rms level of 0.06 K[T_A^*].

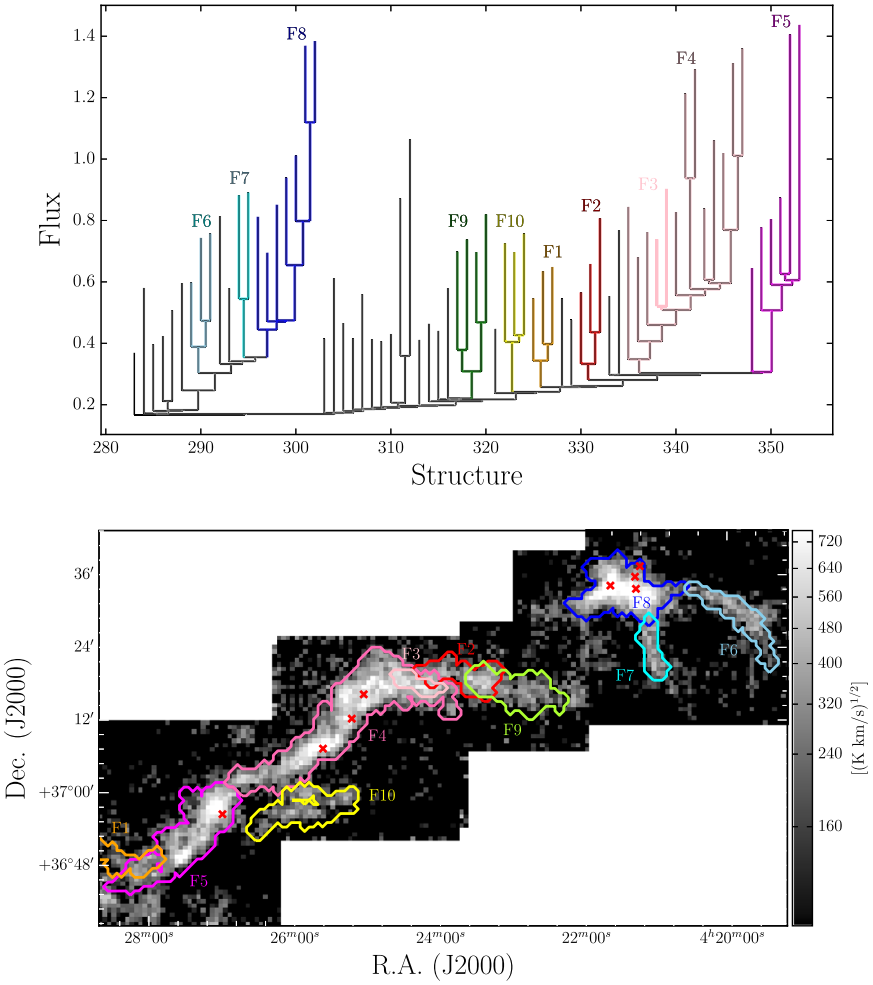

Figure 3. Top: branches and leaves for L1478 identified by dendrogram analysis. The x axis indicates an identification number of a structure in L1478, and the y axis denotes the intensity of each structure in K[T_A^*] . Bottom: leaves in the dendrogram overlaid on the $C^{18}O$(1–0) integrated intensity map (the grayscale image). Each identified leaf in the top panel is drawn in this panel as a filament, named as F1 to F10. Leaves found in the observing boundary are usually noisy structures falsely identified and thus are excluded in further analyses. The red crosses represent the locations of dense cores identified with N_2H^+ data (Section 3.2).

We applied the FellWalker source extraction algorithm (Berry 2015) to the N_2H^+ integrated intensity image to find dense cores. In running this algorithm, only pixels whose intensities are higher than 3σ were considered. The required minimum number of pixels that a core should include to be identified as a real core is seven; that is, it should be larger than one beam size of $56''$. In case there are neighboring peaks, if the difference between the peak value and the minimum value (dip value) is larger than $1\sigma_{\rm rms}$, it is considered as an independent core. With these criteria, we obtained eight cores: three in F4, one in F5, and four in F8.

The masses of the identified dense cores are derived with the integrated intensity of N_2H^+. We calculated the total column density of N_2H^+ following Equation (A4) of Caselli et al. (2002) and converted it into the corresponding H_2 column density with an average abundance of N_2H^+ of $\sim 6.8(\pm 4.8) \times 10^{-10}$ (Johnstone et al. 2010; Lee & Myers 2011). The uncertainties in the N_2H^+ intensities are typically less then 30%, while the uncertainties of excitation temperature and the conversion factor between the column densities of N_2H^+ and H_2 are quite large but less than a factor of 2 (Johnstone et al. 2010). Hence, the uncertainties of dense core masses are less than a factor of 2. The virial masses ($M_{\rm vir}$) are derived with the equation $M_{\rm vir} = k\ R\ \sigma_{\rm tot}^2/G$, where R and σ are the radius and total velocity dispersion of the core, respectively (MacLaren et al. 1988). For simplicity, we used $k = 1$ assuming a density profile of $\rho \propto R^{-2}$, where R is the core radius. The dense cores identified show virial parameters, $\alpha = M_{\rm vir}/M$, between $\sim$0.8 and 2.9. Five dense cores that have $\alpha < 2$ are likely close to a gravitationally bound status. However, we should be careful to interpret the results because the resulting masses have large uncertainties. The information on identified dense cores and calculated masses are listed in Table 2, and the positions and the spectra are presented in Figures 4 and 5.

3.3. Physical Properties of the Identified Filaments

For the 10 filaments identified with the dendrogram technique, we derived physical quantities such as molecular gas mass, length and width, mass per unit length, peak velocity distribution, and nonthermal velocity dispersion.

3.3.1. H_2 Column Density and Mass

We estimated H_2 column density from the $C^{18}O$ column density using the formula (Garden et al. 1991; Pattle et al. 2015)

$$N = \frac{3k_{\rm B}}{8\pi^3 B\mu^2}\frac{e^{hBJ(J+1)/k_{\rm B}T_{\rm ex}}}{J+1}\frac{T_{\rm ex}+\frac{hB}{3k_{\rm B}}}{1-e^{-h\nu/k_{\rm B}T_{\rm ex}}}\int \tau {\rm dv}, \qquad (1)$$

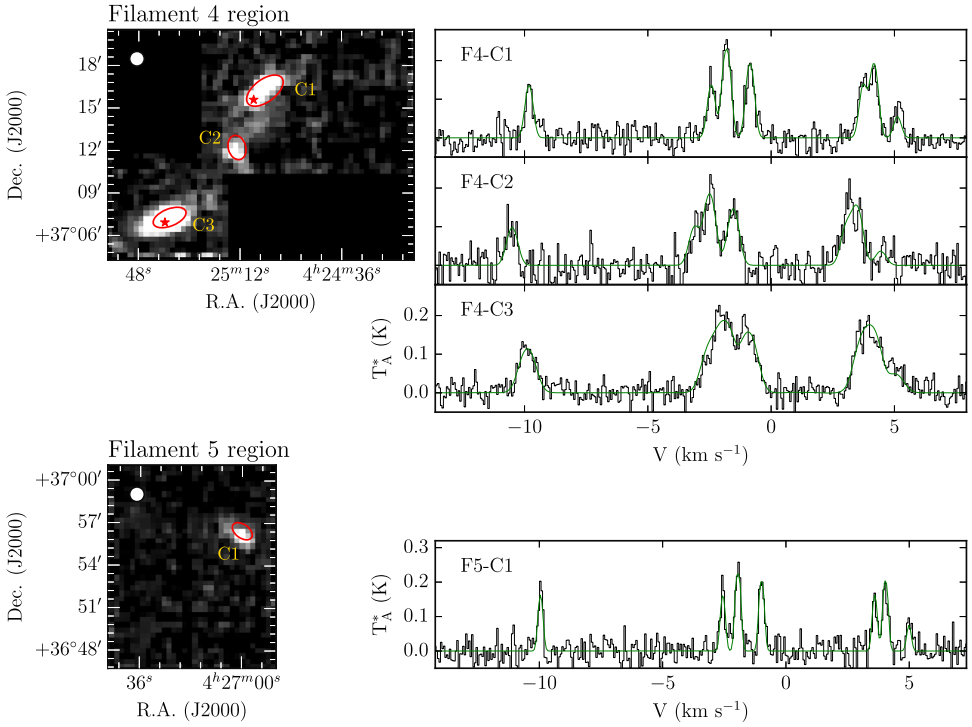

Figure 4. Left: dense cores identified using FELLWALKER are presented with red ellipses on the N_2H^+ integrated intensity maps (moment 0 maps) of Filament 4 and Filament 5. The 56″ FWHM beam at 93.176 GHz is shown by the white circle. The red stars represent positions of YSOs reported by Broekhoven-Fiene et al. (2018). Right: N_2H^+ spectra of dense cores are presented with hyperfine fitting results (green lines).

Table 2
Information on the Identified Dense Cores

Core ID	Position		Size		PA	$V_{peak}(N_2H^+)$	$\Delta V(N_2H^+)$	M_{obs}	α_{vir} [a]	IR Class [b]
	R.A. (hh:mm:ss)	Decl. (dd:mm:ss)	Major (pc)	Minor (pc)	(deg.)	(km s^{-1})	(km s^{-1})	($M_\odot$)		
Filament 4 region										
F4-C1	04:25:03.21	+37:16:14.34	0.39	0.21	126	−1.78	0.35	1.42	1.35	Class 0
F4-C2	04:25:13.10	+37:12:13.32	0.23	0.16	15	−2.47	0.51	0.62	2.88	
F4-C3	04:25:36.96	+37:07:16.54	0.32	0.16	111	−1.85	0.72	1.87	1.86	Class 0/I
Filament 5 region										
F5-C1	04:26:59.95	+36:56:26.66	0.21	0.13	54	−1.92	0.21	0.33	2.45	
Filament 8 region										
F8-C1	04:21:13.02	+37:37:23.74	0.26	0.17	1	−0.50	0.29	1.55	0.77	
F8-C2	04:21:16.44	+37:33:39.67	0.23	0.19	14	−0.32	0.49	1.80	1.04	
F8-C3	04:21:17.10	+37:35:39.73	0.26	0.16	75	−0.41	0.39	0.53	2.74	
F8-C4	04:21:37.71	+37:34:11.82	0.38	0.34	153	−1.24	0.68	2.98	1.63	Class II

Notes.
[a] Virial parameter, α_{vir}, is given by the ratio of M_{vir}/M_{obs}.
[b] F4-C1, F4-C3, and F8-C4 are identified by Broekhoven-Fiene et al. (2018) based on *Spitzer* and *Herschel*, and the classification given here is based on their IR spectral slopes. F4-C3 and F8-C4 are detected in both *Spitzer* and *Herschel*, but F4-C1 is only detected in *Herschel* PACS.

where B is the rotational constant, μ is the permanent dipole moment of the molecule, J is the lower rotational level, and T_{ex} is the excitation temperature. The excitation temperature is calculated following Pineda et al. (2008):

$$T_{ex} = \frac{T_0}{\ln\left(1 + T_0\left(\frac{T_R}{1-e^{-\tau}} + \frac{T_0}{e^{T_0/T_{bg}}-1}\right)^{-1}\right)}, \quad (2)$$

where $T_0 = h\nu/k_B$ and T_{bg} is the cosmic microwave background temperature (2.73 K). We used the radiation temperature of ^{13}CO for T_R with assumptions that C^{18}O and ^{13}CO trace materials with the same excitation temperature and ^{13}CO is optically thick. We derived optical depths τ of ^{13}CO and C^{18}O with the abundance ratio of [^{13}CO/C^{18}O] = 5.5 (Frerking et al. 1982) and the relation

$$\frac{T_{max,C^{18}O}}{T_{max,^{13}CO}} = \frac{1-e^{-\tau_{C^{18}O}}}{1-e^{-\tau_{^{13}CO}}}, \quad (3)$$

where $T_{max,C^{18}O}$ and $T_{max,^{13}CO}$ are the maximum intensities of C^{18}O and ^{13}CO, respectively. In regions far from the main filaments, ^{13}CO is not necessarily optically thick. In this case,

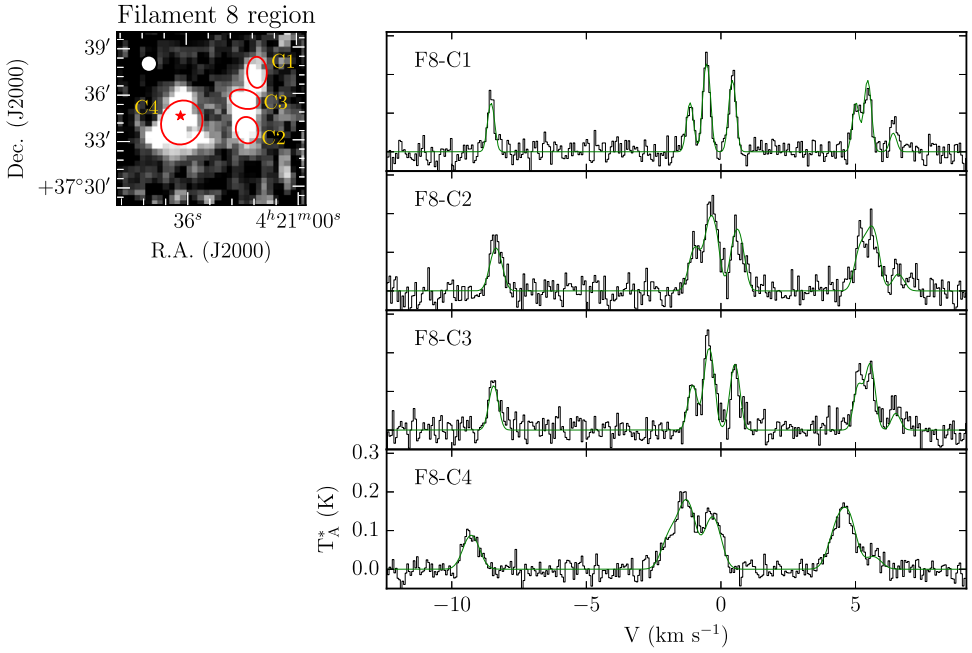

Figure 5. Same as Figure 4 for Filament 8.

we adopted the excitation temperature for their nearest position where $\tau_{^{13}CO} > 1$. The resulting excitation temperature ranges between 5 and 11 K. Imara et al. (2017) derived temperatures from ^{12}CO data and provided ∼7 K for F6 and F7. Our T_{ex} of these two filaments ranges from 5 to 9.5 K, and the average T_{ex} is ∼7 K, which is well matched with that of Imara et al. (2017).

The rightmost integration term of Equation (1) can be written as (Pattle et al. 2015)

$$\int \tau(v)\,\mathrm{dv} = \frac{1}{J(T_{ex}) - J(T_{bg})} \int \frac{\tau(v)}{1 - e^{-\tau(v)}}\, T_{mb}\,\mathrm{dv} \approx \frac{1}{J(T_{ex}) - J(T_{bg})} \frac{\tau(v_0)}{1 - e^{-\tau(v_0)}} \int T_{mb}\,\mathrm{dv},$$

where v_0 is the central velocity, T_{mb} is the observed main beam temperature of the line, and $J(T)$ is the source function, $J(T) = T_0/(e^{T_0/T} - 1)$ and $T_0 = h\nu/k_B$, and T_{ex} and T_{bg} are the excitation temperature and cosmic microwave background temperature as described in Equation (1). To calculate $\int T_{mb}\mathrm{dv}$, we used the area under the fitted Gaussian function. Since most of the spectra have a shape of a Gaussian profile, the difference between the area under the fitted Gaussian function and the integrated T_{mb} within the velocity range of $v_{cen} \pm \triangle v/2$, where v_{cen} and $\triangle v$ are the central velocity and line width of the Gaussian fitting results, respectively, is found to be less than 5%.

N_{H_2} from $N_{C^{18}O}$ is calculated with the conversion factor $N_{H_2}/N_{^{12}CO} = 1.1 \times 10^4$ (Pineda et al. 2010) and the abundance ratios $^{12}CO/^{13}CO = 69$ (Wilson 1999) and $^{13}CO/C^{18}O = 5.5$ (Frerking et al. 1982). The derived H_2 column density distribution is shown in panel (b) of Figure 6.

We also estimated the H_2 column density from *Herschel* data to check whether the value derived with $C^{18}O$ is reliable or not. First, 250 μm, 350 μm, and 500 μm *Herschel* data were convolved to the 44″ pixel size and then coaligned on the TRAO $C^{18}O$ and ^{13}CO pixel grid. Second, we derived spectral energy distribution fits from 250 μm, 350 μm, and 500 μm data for each pixel position with a simple dust emission model, $F_\nu = \kappa_\nu \times B(\nu, T)\times$ column density. A dust opacity law of $\kappa_\nu = 0.1(\nu/1000\ \mathrm{GHz})^\beta\ \mathrm{cm^2 g^{-1}}$ is assumed with fixed dust emissivity index β of 2 (Draine & Lee 1984; Schnee et al. 2010), and the standard mean molecular weight, μ, of 2.86 is used to calculate the H_2 column density (Kauffmann et al. 2008).

The measured H_2 column densities from $C^{18}O$ and *Herschel* data are compared in Figure 7. It appears that $N_{H_2}^{C^{18}O}$ is smaller than $N_{H_2}^{Herschel}$ by a factor of ∼2, but with good linear correlation.

The multiple velocity components of filaments can cause $N_{H_2}^{C^{18}O}$ to be smaller than $N_{H_2}^{Herschel}$. The spectra with multiple velocity components are presented in Figure 2 and the Appendix (Figures 14 and 15), and multiple velocity components of filaments are overlapped in the plane of the sky. In this area, H_2 column density from $C^{18}O$ is derived separately for each filament components, while N_{H_2} from *Herschel* dust emission is summed for the different filaments. Hence $N_{H_2}^{C^{18}O}$ becomes less than $N_{H_2}^{Herschel}$. We should also add the other well-known facts that the CO depletion and dissociation can cause differences between H_2 column densities derived with the two methods. At high densities of $n_{H_2} \gtrsim 10^5\ \mathrm{cm^{-3}}$ and low dust temperatures of <20 K, CO is depleted through freeze-out onto dust grains. Besides, Herschel is sensitive to the large-scale structure of the cloud, where the dust is warmer and CO may be, at least partially, photo-dissociated, so it is not properly tracing this outer zone of the cloud (e.g., Caselli et al. 1999; Tafalla et al. 2004; di Francesco et al. 2007; Spezzano et al. 2016).

The difference between $N_{H_2}^{C^{18}O}$ and $N_{H_2}^{Herschel}$ can also be affected by the use of some uncertain parameters. The typical error of H_2 column density measured from *Herschel* data is a factor of 2, which is mainly caused by the uncertainty of the dust opacity law. In the case of N_{H_2} from $C^{18}O$, it is more

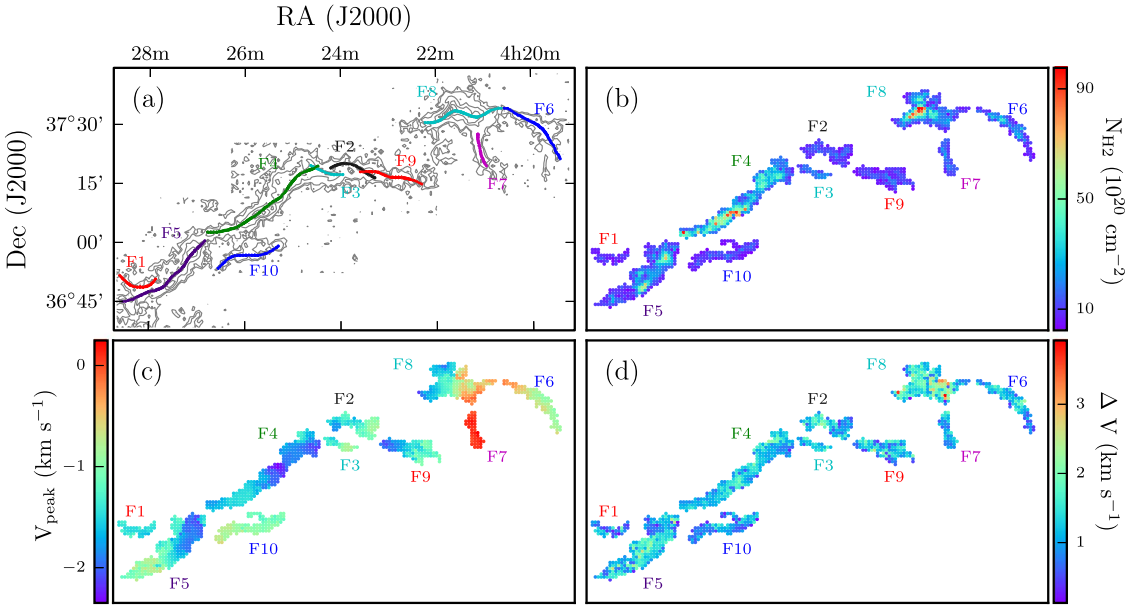

Figure 6. (a) Locations of 10 identified filaments (skeletons) on top of the integrated intensity map of $C^{18}O$ (the same as the contour map in the bottom panel of Figure 2; contours are 2, 3, 6, 9, ⋯, 18 × σ in K km s^{-1}). (b)–(d) H_2 column density, velocity field, and line width maps of each filament. V_{peak} and ΔV (linewidth) are quantities derived by the Gaussian fitting method. A small offset is given to the original position of each filament to avoid spatial overlaps and distinguish them from each other.

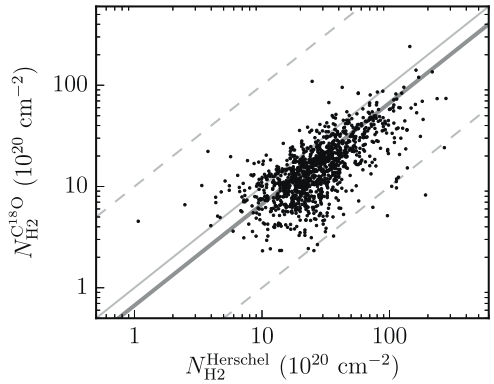

Figure 7. Comparison of H_2 column densities from $C^{18}O$ and *Herschel* data. The solid thin gray line superimposed indicates where $N_{H_2}^{C^{18}O}$ and $N_{H_2}^{Herschel}$ are identical, and the two dashed lines show where the ratio $N_{H_2}^{C^{18}O}/N_{H_2}^{Herschel}$ is 10 and 0.1. The thick solid line presents the least squares fit result.

complicated because the conversion factor of CO to H_2 and the ratios of CO/^{13}CO and ^{13}CO/C^{18}O vary by a factor of up to 5 according to the metallicity, column density, and temperature gradients (see Pineda et al. 2010; Bolatto et al. 2013, and references therein). Hence, the uncertainty of N_{H_2} measured from $C^{18}O$ is likely to be a factor of a few, and we can conclude that the resulting $N_{H_2}^{C^{18}O}$ and $N_{H_2}^{Herschel}$ are well matched with each other within a range of uncertainty.

The H_2 column density measured with $C^{18}O$ ranges over 2–100 × 10^{20} cm^{-2}, and the H_2 mass of each identified filament is ∼10 to 200 $M_\odot$. The estimated mass of each filament is tabulated in Table 3.

3.3.2. Length and Width

We estimated the filament's length along the skeleton without any correction of the projection effect. Filament skeletons are determined in the following procedures. First, we made moment 0 images for each filament, then applied FILFINDER, which uses the Medial Axis Transform method, to the moment 0 images for each filament. The Medial Axis Transform method gives a skeleton that is the set of central pixels of inscribed circles having maximum radius (Koch & Rosolowsky 2015). The skeletons determined with this process are well matched with the skeleton obtained with DISCRETE PERSISTENT STRUCTURES EXTRACTOR (DISPERSE). The DISPERSE algorithm finds the skeleton by connecting the critical points of maxima or saddle points that have a zero gradient in the map and identifies skeletons of filaments (Sousbie 2011). There is a slight deviation among the skeletons obtained between the two algorithms that is less than two pixels in size in most cases. The skeletons of identified filaments with their IDs are shown in panel (a) of Figure 6. Lengths of filaments in L1478 range from ∼3′ to 11′, which correspond to about 0.4 pc to 1.4 pc at the distance of 450 pc.

The filament width is measured from the H_2 column density map (see Section 3.3.1 and Figure 6) of each filament. We made a radial profile of H_2 column density versus distance from the skeleton, applied Gaussian fitting, and derived the FWHM as the filament's width.

The resulting lengths and widths of the filaments are listed in Table 3. As can be seen, the width ranges from ∼0.1 to 0.2 pc. This is consistent with the typical filament width of 0.1 pc that is shown in *Herschel* images (Arzoumanian et al. 2011). But it should be considered here that our spatial resolution of $C^{18}O$ is ∼47″, corresponding to 0.1 pc at the distance of 450 pc, and thus our result for the width may be affected by our observing resolution in space.

3.3.3. Mass per Unit Length

With the mass and length of the filament, we calculated the mean of the mass per unit length, M_{line}. We simply divided the mass of a filament by its length given in Sections 3.3.1 and 3.3.2,

Table 3
Physical Properties of Filaments

Fil. ID (1)	V_{peak} Range (2)	$\bar{\sigma}_{tot}$ (3)	L (4)	W (5)	M (6)	M_{line} (7)	M_{line}^{crit} (8)	$\lvert\nabla V_{peak}\rvert$ (9)	cores (10)	YSOs (11)
1	−1.7 to −1.2	0.18	0.45	0.10	6.9	15.3	14.8 ± 12.3	1.12	N/A	
2	−1.9 to −0.8	0.24	0.51	0.12	17.8	34.7	25.6 ± 17.4	1.90	N/A	
3	−1.6 to −0.8	0.24	0.35	0.07	9.4	26.5	27.6 ± 12.1	2.61	N/A	
4	−2.3 to −1.3	0.24	1.40	0.08	216.1	154.1	25.7 ± 12.9	0.69	3	2
5	−2.2 to −0.6	0.25	1.12	0.19	85.6	76.5	28.3 ± 19.7	1.28	1	
6	−1.0 to −0.2	0.22	0.83	0.10	25.7	30.9	22.0 ± 14.7	0.89	N/D	
7	0.0 to 0.3	0.21	0.35	0.13	12.3	34.9	20.0 ± 10.3	0.63	N/D	
8	−2.1 to −0.1	0.31	0.87	⋯	127.8	147.6	45.0 ± 33.7	2.26	4	1
9	−2.1 to −1.0	0.23	0.66	0.14	20.0	30.1	23.5 ± 7.5	1.57	N/A	
10	−1.3 to −0.6	0.18	0.70	0.08	19.3	27.5	14.9 ± 9.7	0.85	N/A	

Note. (1) Filament ID. (2) The largest and smallest V_{peak} in km s^{-1}. (3) Averaged total velocity dispersion from the $C^{18}O$ line widths in km s^{-1}. (4) Length of filament measured from the eastmost (or northmost) point to the westmost (or southmost) point of the skeleton in parsecs. (5) Filament width in pc, i.e., FWHM of radial profile of H_2 column density. (6) H_2 mass of filament in $M_\odot$. (7) Mass per unit length of filament in $M_\odot$ pc^{-1}. (8) Effective critical mass per unit length of filament derived with the mean total velocity dispersion in $M_\odot$ pc^{-1} (see Section 4.2). (9) Mean velocity gradient of filament in km s^{-1} pc^{-1}. (10) Number of dense cores identified with N_2H^+ data. F1, F2, F3, F9, and F10 are not observed with N_2H^+. F6 and F7 are observed with N_2H^+, but no emission is detected at the rms level of 0.06 KT_A^*. (11) YSOs identified with *Spitzer* and *Herschel* (Broekhoven-Fiene et al. 2018).

and thus the M_{line} shown here is the averaged mass per unit length of the filament. The mass per unit length of the filaments in L1478 is estimated to range from ∼20 to 150 $M_\odot$ pc^{-1}.

3.3.4. Global Velocity Field

Intensity-weighted mean velocity (moment 1) and velocity dispersion (moment 2) maps are very useful for understanding the global velocity properties of molecular clouds, but they may not be appropriate for studying the kinematics of filaments showing multiple velocity components that are due to their spatial overlaps. Hence, we carried out Gaussian fitting for the $C^{18}O$ spectra to extract velocity information of the filaments.

The global continuous velocity distribution and gradient in the filaments can be seen in the peak velocity distribution map, panel (c) in Figure 6. In Section 3.1, we mentioned that F1 to F5 are from one stem though they are found as independent leaves, and this is also true for F6 to F8. Those filaments are identified as independent filaments because they have a maximum of 2σ higher than the saddle point and they are all connected to each other. The peak velocity map shows that they are spatially and kinematically continuous. Especially, it is shown that F6 and F7 are continuously connected with F8 in the velocity space as well as in the plane of the sky, indicating they have a clear hub–filament structure, that is, dense star-forming hubs with multiple filaments.

Information for the velocity distribution of each filament is tabulated in Table 3 as quantities of V_{peak} ranges and gradients ($|\nabla V_{peak}|$) of filaments. Figure 8 shows the peak velocity distribution along the skeleton of each filament. The slope (velocity gradient) is different from filament to filament and seems to be intrinsic to each filament, although no inclination correction has been applied. The variation of V_{peak} ($\triangle V_{peak}$) changes between ∼0.3 and 2 km s^{-1} for each filament. F5 and F8 have the largest $\triangle V_{peak}$ of ∼2 km s^{-1}, and F7 has the smallest $\triangle V_{peak}$ of 0.3 km s^{-1}. The mean velocity gradient ($|\nabla V_{peak}|$) ranges from about 0.6 to 2.6 km s^{-1} pc^{-1}, and F3 shows the largest $|\nabla V_{peak}|$ of ∼2.6 km s^{-1} pc^{-1}.

We can see two clear kinematic properties of filaments. The one is the coherence of velocities of filaments; that is, every filament, even F8, which has a hub–filament shape, has a continuous V_{peak} along the skeletons. The other one we notice is that some different velocity components appear (drawn with thick gray lines for F2, F4, F5, F6, and F9). We will discuss more the different velocity components in Section 4.

3.3.5. Nonthermal Velocity Dispersion

Nonthermal velocity dispersion (σ_{NT}) can be calculated as follows:

$$\sigma_{NT} = \left(\sigma^2 - \frac{k_B T}{\mu m_H}\right)^{1/2} \quad (4)$$

where σ is the velocity dispersion derived from the FWHM, k_B is the Boltzmann constant, T is the gas temperature, μ is the mean molecular weight of $C^{18}O$ and N_2H^+, and m_H is the mass of the atomic hydrogen.

The FWHM values for $C^{18}O$ and N_2H^+ were obtained from Gaussian fits to those spectra. In the case of N_2H^+ spectra, seven hyperfine components were simultaneously fitted with seven Gaussian forms at once using their line parameters given by Caselli et al. (1995). The gas temperature is assumed to be the same as T_{ex}, which is derived in Section 3.3.1.

Figure 9 shows the nonthermal velocity dispersions in all of our identified filaments and dense cores. Except for F8, σ_{NT}/c_s of every filament peaks at the transonic regime (∼1.5). Though F1 has a peak of σ_{NT}/c_s between 0.5 and 1.0, the portion of the transonic nonthermal velocity dispersion is about the same as that of the subsonic components (47% each). F8, which has YSOs, appears to have ∼51% of spectra of supersonic velocity dispersions.

Nonthermal velocity dispersions measured from the dense core tracer N_2H^+ (denoted with squares of various colors) are smaller than those from $C^{18}O$, either subsonic or transonic. The histogram of σ_{NT}/c_s from N_2H^+ (presented with red color) shows that σ_{NT}/c_s from N_2H^+ of F4 and F8 peaks at the

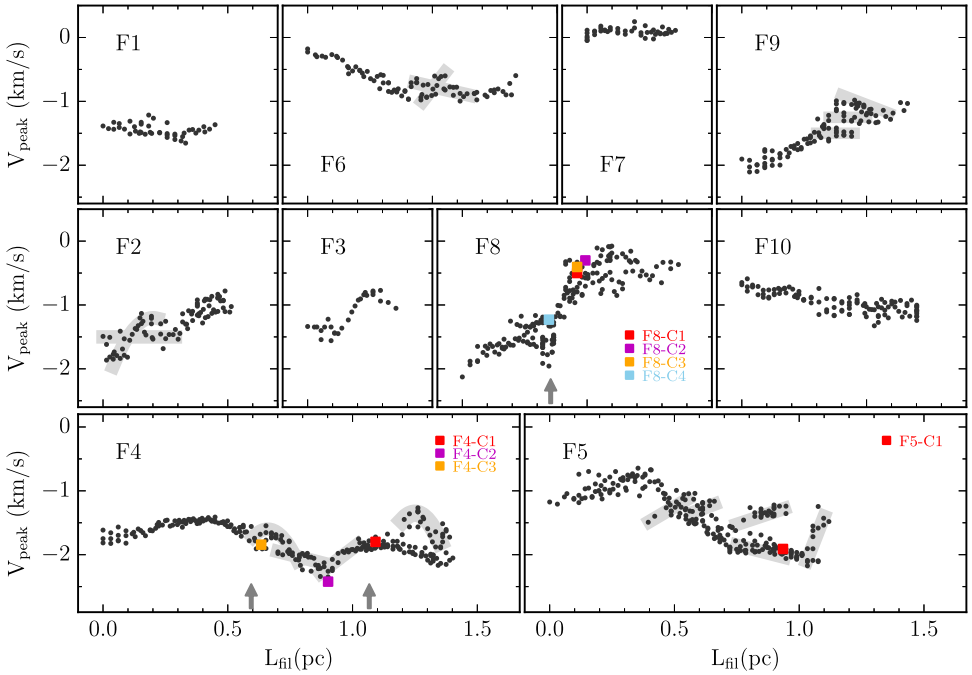

Figure 8. Velocity structures along the filaments. $L_{\rm fil}$ is calculated along the skeleton points (Section 3.1) from the eastmost point of each filament. $V_{\rm peak}$ from $C^{18}O$ is presented with solid black dots. $V_{\rm peak}$ of each core denoted here is derived from the averaged N_2H^+ (see Figures 4 and 5). The thick gray lines are drawn to highlight some different velocity components. The YSOs reported by Broekhoven-Fiene et al. (2018) are presented with gray arrows in their positions along the skeleton.

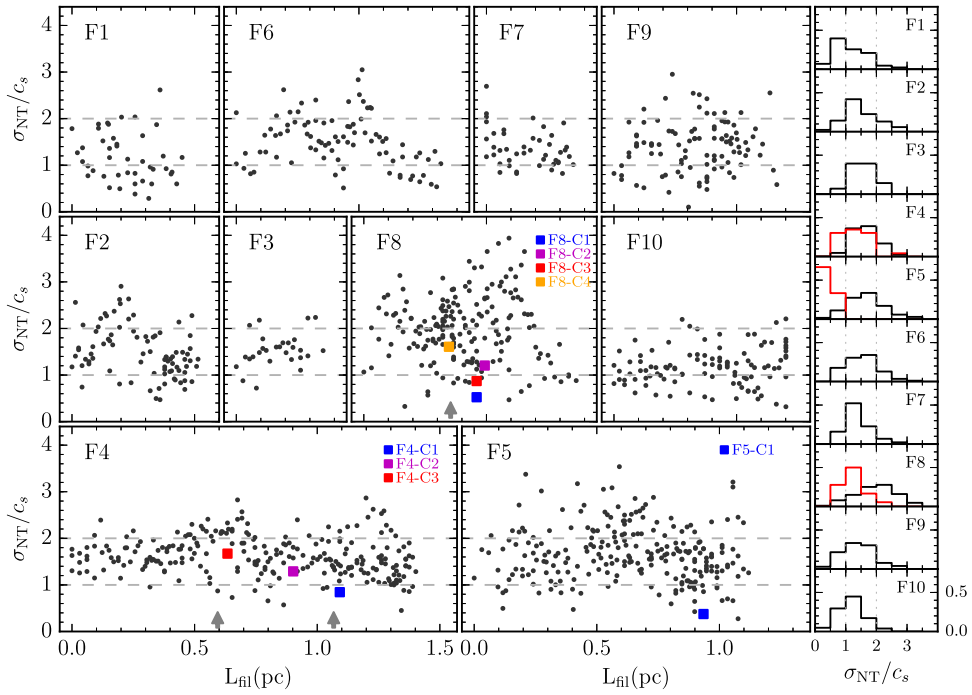

Figure 9. Velocity dispersions in all identified filaments and dense cores. Left panels: nonthermal velocity dispersions normalized by the local sound speed as a function of the position along each filament. The $\sigma_{\rm NT}/c_{\rm s}$ derived from $C^{18}O$ is denoted with solid black dots. The $\sigma_{\rm NT}/c_{\rm s}$ derived from the averaged N_2H^+ spectrum of each dense core (see Figures 4 and 5) are presented with different colors of squares. The positions of YSOs reported by Broekhoven-Fiene et al. (2018) are presented with gray arrows. Right panels: normalized histograms of $\sigma_{\rm NT}/c_{\rm s}$. The $\sigma_{\rm NT}/c_{\rm s}$ derived from line widths of $C^{18}O$ and of N_2H^+ are presented with black and red, respectively. Here, histograms of $\sigma_{\rm NT}/c_{\rm s}$ derived from N_2H^+ are not from the averaged spectrum but from every detected N_2H^+ spectra (signal-to-noise ratio S/N > 5).

transonic regime ($1 \lesssim \sigma_{\rm NT}/c_{\rm s} \lesssim 2$), while that of F5 peaks at subsonic values. F4 shows similar velocity dispersions in filaments traced by $C^{18}O$ and in dense cores traced by N_2H^+, but F5 and F8 have different distributions of $\sigma_{\rm NT}^{\rm C^{18}O}$ and $\sigma_{\rm NT}^{\rm N_2H^+}$.

3.3.6. Chemical Evolution of Dense Cores

Integrated intensity maps of N_2H^+, $C^{18}O$, and SO molecular lines are presented in Figure 10 with the dense cores identified in Section 3.2. SO is known as one of the most sensitive

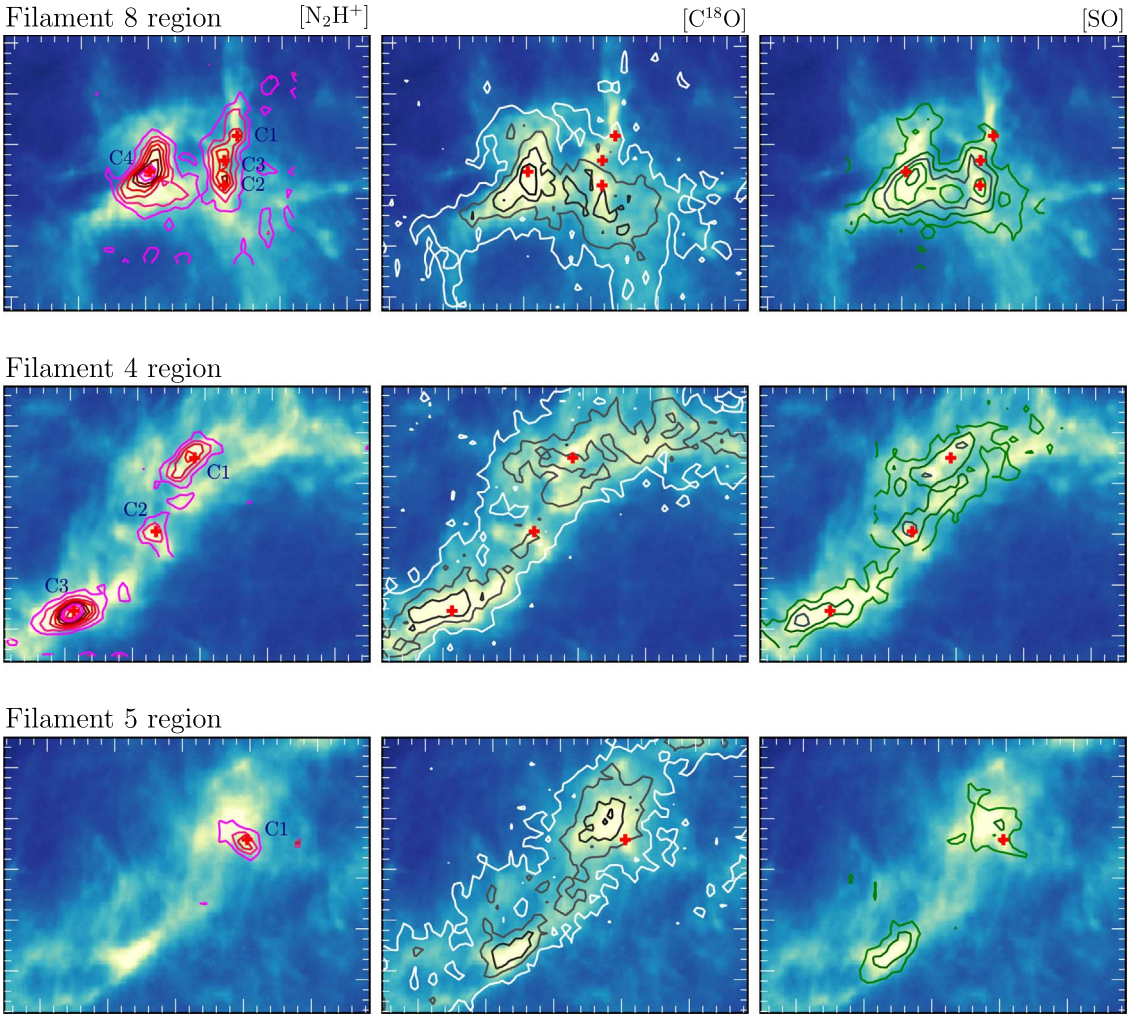

Figure 10. Integrated intensity contour maps of N_2H^+ (left), $C^{18}O$ (middle), and SO (right) on the *Herschel* 250 μm background image. Contours are at every 3σ interval from 3σ. The N_2H^+ peak positions of identified dense cores are presented with red crosses.

molecules of molecular depletion, and N_2H^+ is known to survive much longer at high density when CO becomes depleted in the gas phase (e.g., Tafalla et al. 2006).

As can be seen in the maps, N_2H^+ traces more compact regions than $C^{18}O$ and SO. The chainlike structure of the cores can be seen in the F8 and F4 regions. F8-C1, F8-C2, and F8-C3 and F4-C1, F4-C2, and F4-C3 stand in lines, and their N_2H^+ emission contours show a chainlike structure, which is, however, not clear in $C^{18}O$ and SO because of their possible depletion.

In the F8 region (top panels), four dense cores are identified. F8-C1 and F8-C3 show relatively weak emissions in the three molecular lines of N_2H^+, $C^{18}O$, and SO. Meanwhile, F8-C2 has a SO condensation at the peak position of N_2H^+. F8-C4, which is the largest and brightest core, contains a class II object. Hence, F8-C4 can be the most evolved core in this filament, and F8-C2 seems to be relatively younger than F8-C4.

In the F4 region (middle panel), three dense cores are found. $C^{18}O$ is extended from the southeast to the northwest, but there is no N_2H^+ or SO emission toward the northwest. F4-C3 is the largest core with the brightest and centrally peaked N_2H^+ emission in the F4 region, but $C^{18}O$ and SO are not as peaked as N_2H^+. This is the same for F4-C1, which has a centrally peaked N_2H^+ but not $C^{18}O$ and SO. On the contrary, F4-C2, which has the weakest N_2H^+ emission, is similarly peaked in three lines. Hence, F4-C2 appears to be the youngest core in the Filament 4 region.

In the F5 region (bottom panels), only one core is found. Peaks of $C^{18}O$ and SO show a slight offset from the N_2H^+ peak and thus can be depleted. This indicates that F5-C1 is not a young but an evolved core. On the other hand, at the southeastern region of F5-C1, where no N_2H^+ emission is detected, $C^{18}O$ and SO emissions are clearly detected, indicating that this region is at an earlier stage.

The chemical differences between cores that form in a filament indicate that they are at different stages of evolution. Lee & Myers (2011) carried out various molecular line observations toward several tens of starless cores, and they found that the column density increases in a sequence of core evolution in which the earliest stage is static cores, and the next is expanding or oscillating cores, and the most evolved one is contracting cores. To probe the relation between column density and evolution status, we compared the H_2 column density between the cores. The youngest cores in F4 and F8 are F4-C2 and F8-C2, and they have lower H_2 column densities than other dense cores, which agrees with the result of Lee & Myers (2011) that cores with higher H_2 column density tend to be more evolved than others. However, the internal motions

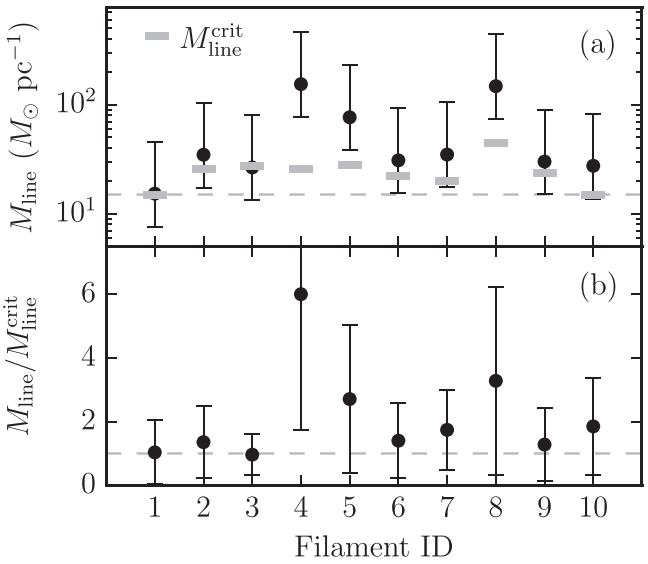

Figure 11. Criticality of observed filaments. (a) The mass per unit length ($M_{\rm line}$) is presented with solid dots, and the effective critical mass per unit length derived with the average $\sigma_{\rm tot}$ for each filament is presented with a gray bar. The gray dashed line denotes the equilibrium value ($\sim$15 $M_\odot$ pc^{-1}) for an isothermal cylinder in pressure equilibrium at 10 K. The error bars indicate the factor of two uncertainties of $M_{\rm line}$. (b) Ratios of mass per unit length to effective critical mass per unit length. The gray dashed line indicates the line where $M_{\rm line}$ and $M_{\rm line}^{\rm crit}$ are identical.

such as static, expanding or oscillating, and contracting motions in each evolutionary stage are not clearly related to the evolutionary stage in our dense cores. In Filament 4, the youngest core F4-C2 does not show a clear infall signature, but the other cores F4-C1 and F4-C3 show clear infall motions, indicating the contraction of cores. On the contrary, in Filament 8, the most evolved core F8-C4 does not show any infall signature, but F8-C1 and F8-C2, which are younger than F8-C4, show a blue asymmetry, showing contraction. However, because of our small number of dense cores, it is difficult to conclude that the internal motions of cores are not correlated with the evolutionary stage of cores.

4. Discussion

4.1. Fibers, Building Blocks of Filaments?

Recent molecular line observations of filaments with higher spatial and spectral resolutions lead us to confirm the presence of fibers. Hacar et al. (2018) proposed that all filaments are bundles of fibers that have a typical length and width of $\sim$0.5 pc and 0.035 to 0.1 pc, respectively, and are velocity-coherent and characterized by transonic internal motions. Fibers are found in various star-forming environments, from low- to high-mass star-forming clouds (e.g., Hacar et al. 2013, 2016, 2017, 2018; Maureira et al. 2017; Clarke et al. 2018; Dhabal et al. 2018). Interestingly, Hacar et al. (2018) showed that the mass per unit length of the total filament has a linear correlation with the surface density of fibers and suggested a unified star formation scenario for the isolated, low-mass and the clustered, high-mass stellar populations where the initial number density of fibers may determine the star-forming properties of molecular clouds and filaments. Our beam size ($\sim$0.1 pc at the distance of 450 pc) is comparable to the width of the fibers, and it is smaller than the typical lengths of fibers. Besides, our velocity resolution is enough to check the presence of fibers.

In Figure 8, the $V_{\rm peak}$ distribution along the skeleton appears to be coherent in each filament, but fiber-like velocity structures can be seen in every filament, especially in F2, F4, F5, and F6. F4, which has YSOs and dense cores, seems to have fibers weaving together at positions $L_{\rm fil} \sim$ 0.6, 0.9, and 1.2 pc (indicated with thick gray curves in Figure 8). It is interesting that the junction of fibers with slightly different velocities is consistent with the position of dense cores. F5 looks like there is one long main filament, and shorter fibers are interlaced with the main filament. Actually, at the northwestern part of F5 (at $L_{\rm fil} \sim$ 0.7 to 1.0), a clear double peak is shown in the C^{18}O spectra, and the difference in peak velocities is $\sim$0.5 km s^{-1}. In F2, F6, and F9, the braided fibers can be found, too. These three filaments seem to be composed of two parallel fibers that meet each other at the center of the filament. F8 has a hub-like morphology, but its velocity structure also shows the presence of fibers.

What we can see with our data is still limited because of its poor spatial resolution, but one noticeable thing is that the filaments having YSOs and dense cores show more clear evidence for the presence of fibers than other filaments do. F4 and F5 look like they have more fibers than other filaments in L1478, and furthermore they are gravitationally unstable and have YSOs and dense cores. In other words, the peak velocity distributions of filaments in L1478 indirectly indicate that filaments are made of fibers, and the filaments that are gravitationally collapsing show a denser and finer distribution of fibers. These results support the star formation scenario suggested by Hacar et al. (2018) that filaments are bundles of velocity-coherent fibers and fibers are an arbiter of star formation in molecular clouds in a sense.

4.2. Are the Filaments in L1478 Gravitationally Bound?

The ubiquity of filaments indicates that the filament is an indispensable structure in the star formation process. André et al. (2010) proposed a core formation scenario based on the *Herschel* Gould Belt Survey observation that long and thin filaments are made first in the molecular clouds and then prestellar cores form by hierarchical fragmentation of gravitationally unstable filaments. The equilibrium line mass or mass per unit length for an isothermal, unmagnetized filament in pressure equilibrium is $M_{\rm line,eq}^{\rm unmag} = 2c_{\rm s}^2/G$, where $c_{\rm s}$ is the isothermal sound speed (Ostriker 1964; Inutsuka & Miyama 1992, 1997). The critical value at 10 K is $\sim$15 $M_\odot$ pc^{-1}, and a filament with larger $M_{\rm line}$ than $M_{\rm line,eq}$ becomes supercritical and undergoes gravitational contraction.

Filaments in L1478 have a mass per unit length of $\sim$20–150 $M_\odot$ pc^{-1}, which is larger than the equilibrium mass per unit lengths. This means that every filament in L1478 is supercritical and will collapse gravitationally, and dense cores can be formed by gravitational fragmentation along the filaments. However, in this case, nonthermal components such as turbulent motions as well as magnetic field are not considered. Hence, we derived the effective critical mass per unit length that includes nonthermal motions, $M_{\rm line}^{\rm crit} = 2\bar{\sigma}_{\rm tot,3d}^2/G = 2(\sqrt{3}\,\bar{\sigma}_{\rm tot})^2/G$, where $\bar{\sigma}_{\rm tot}$ is the average total velocity dispersion of a filament (e.g., Arzoumanian et al. 2013; Peretto et al. 2014). The calculated $M_{\rm line}^{\rm crit}$ with $\bar{\sigma}_{\rm tot}$ is tabulated in Table 3 and presented in panel (a) of Figure 11 with a thick gray bar. The ratio, $M_{\rm line}/M_{\rm line}^{\rm crit}$, is given in panel (b) of Figure 11.

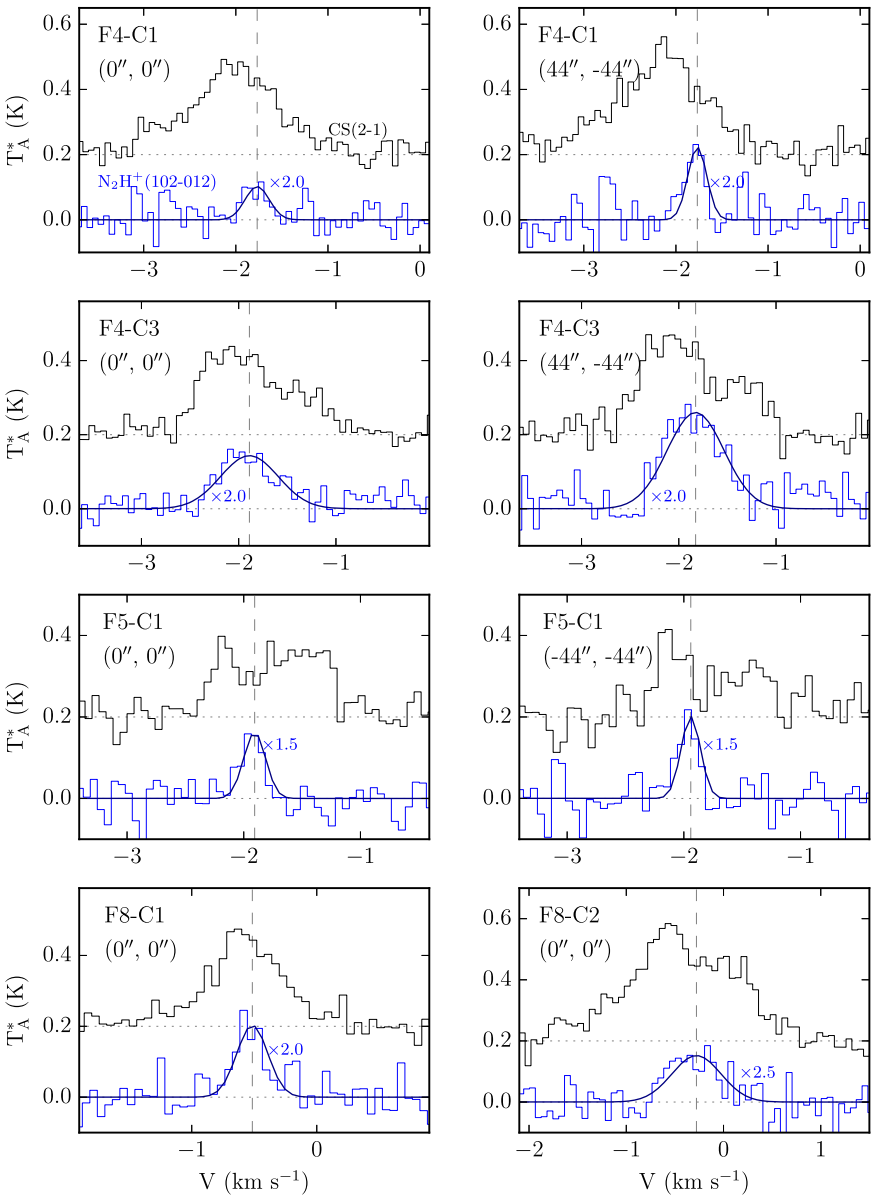

Figure 12. Infall asymmetric profiles toward dense cores in the supercritical filaments F4, F5, and F8. Averaged CS(2–1) and N_2H^+ (102–012) spectra toward dense cores are drawn with black and blue histograms, respectively. Offsets from the core center are given in the top left corner of each panel. The blue solid curve and gray dashed vertical lines are the hyperfine fitting line and central velocity of cores, respectively.

With $M_{\rm line}^{\rm crit}$, all filaments in L1478 are close to critical. The three filaments, F4, F5, and F8, are highly critical. This is consistent with the fact that the high-density tracer of N_2H^+ is detected and YSOs are found in these filaments only (Broekhoven-Fiene et al. 2018).

To see whether there are any inward motions from the gravitationally bound filaments to the dense core, we check the CS(2–1) and N_2H^+(1–0) line profiles. Blue asymmetry in spectral profiles is generally used to identify infall signatures of dense cores and molecular clouds (e.g., Leung & Brown 1977; Lee et al. 2001). In centrally concentrated cores, the foreground gas appears to be absorbed in optically thick lines. If inward motions prevail, the absorption of foreground gas becomes redshifted, and the optically thick emission line appears to be brighter in the blue peak. As shown in Figure 12, among the eight dense cores found from N_2H^+ data, F4-C1, F4-C3, F5-C1, and F8-C2 show the blue asymmetry in the CS(2–1) line profile, implying the existence of gas infalling motions, which is consistent with their status of criticality.

4.3. Do Cores Form by Collisions of Turbulent Flows?

Turbulent motions in filaments and dense cores are important to the formation of filaments and dense cores. Numerical simulations of supersonic turbulence gave a result generating dense structures like sheets, filaments, and cores (e.g., Padoan et al. 2001a; Xiong et al. 2017; Haugbølle et al. 2018). Padoan et al. (2001a) proposed that filaments can form by collision of turbulent flows, and dissipation of turbulence makes the dense cores. Following this colliding model, the filaments and the dense cores may have supersonic and subsonic motions, respectively. To probe this dense core formation scenario, we checked the kinematic properties of filaments and dense cores.

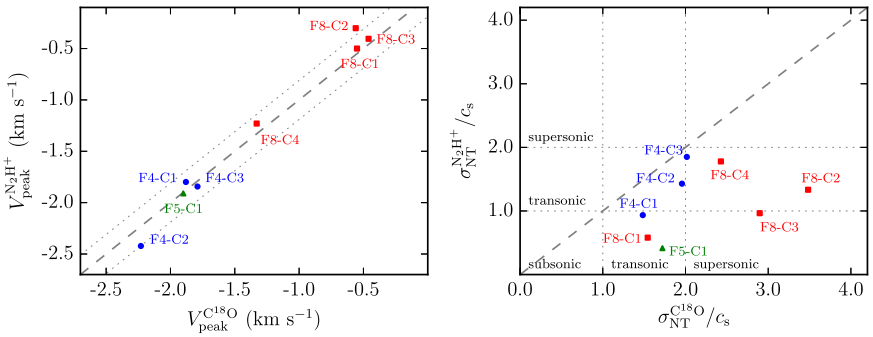

Figure 13. Left: peak velocity of dense cores traced by N_2H^+ and surrounding materials of filaments traced by $C^{18}O$. The mean error in $V_{\rm peak}$ is about 0.02 km s^{-1} for both N_2H^+ and $C^{18}O$, which is comparable to or smaller than the point size. The gray dashed and dotted lines indicate the identical line and its line displaced by the sound speed (about 0.19 km s^{-1} at 10 K). Right: nonthermal velocity dispersion of dense cores traced by N_2H^+ and surrounding materials of filaments traced by $C^{18}O$. The gray dashed line indicates that $\sigma_{\rm NT}^{\rm N_2H^+}$ and $\sigma_{\rm NT}^{\rm C^{18}O}$ are identical. Cores in F4, F5, and F8 are presented with blue circles, green triangles, and red squares, respectively.

First of all, as shown in Figure 8, the $V_{\rm peak}$ distributions between dense cores and the surrounding material of filaments in F4, F5, and F8 are well matched with each other. This can be seen more clearly in the left panel of Figure 13. The peak velocity and velocity dispersion of dense cores and surrounding filament gas were derived with N_2H^+ and $C^{18}O$ spectra, respectively. In the left panel of Figure 8, the peak velocity of the dense core is plotted with that of the surrounding filament gas. Every dense core has a peak velocity identical to that of the filamentary material within the total velocity dispersion traced by $C^{18}O$. Hence, we can conclude that there is no systemic velocity drift between the dense core and the surrounding material. This result is similar to that of previous studies, in which no systemic velocity difference was found between the dense cores and surrounding gas (e.g., Kirk et al. 2007; Hacar & Tafalla 2011; Punanova et al. 2018).

The nonthermal velocity dispersions of filaments and dense cores are presented in sound speed ($c_{\rm s}$) scale in the right panel of Figure 13. As shown in Figure 9, $\sigma_{\rm NT}^{\rm C^{18}O}$ is larger than $\sigma_{\rm NT}^{\rm N_2H^+}$ for every dense core. There are four dense cores that have transonic $\sigma_{\rm NT}^{\rm N_2H^+}$ (F4-C2, F4-C3, F8-C2, and F8-C4) and two dense cores that have subsonic $\sigma_{\rm NT}^{\rm N_2H^+}$ (F5-C1 and F8-C1). The other two dense cores (F4-C1 and F8-C3) have N_2H^+ velocity dispersions in the borderline between the transonic and subsonic.

One noticeable thing is that the relationships of $\sigma_{\rm NT}^{\rm C^{18}O}$ and $\sigma_{\rm NT}^{\rm N_2H^+}$ are different from filament to filament; that is, dense cores that are surrounded with materials in supersonic motion in F8 still have subsonic or transonic motions, while the velocity dispersions of dense cores in F4 become as large as that of their surrounding filament (F4). This different motion between dense cores and surrounding material in filaments can be seen in the histogram of Figure 9, too. The nonthermal velocity distribution of N_2H^+ and $C^{18}O$ in F4 peaks at transonic, but that of N_2H^+ in F8 peaks at transonic, while that of $C^{18}O$ peaks at supersonic. Filament 5 has only one dense core, F5-C1, which appears to be subsonic, $\sigma_{\rm NT}^{\rm N_2H^+} < 0.5c_{\rm s}$, while the less dense material is transonic, $\sigma_{\rm NT}^{\rm C^{18}O} \sim 1.5c_{\rm s}$.

The difference between F4 and F8 implies that the dense cores in F4 and F8 can be formed by different processes. The two filaments are both supercritical, and their velocity fields indicate mass flows along the filament in the case of F4 and from filaments to hub in the case of F8. However, their morphologies and dynamical properties are totally different. F4 has a single long filament shape, but F8 has a hub-like morphology. The dense cores and surrounding material of F4 are both subsonic or transonic, while $\sigma_{\rm NT}^{\rm C^{18}O}$ of F8 are transonic or supersonic, but $\sigma_{\rm NT}^{\rm N_2H^+}$ are still subsonic or transonic. Hence, dense cores in F8 may be formed by collision of turbulent flows (Padoan et al. 2001b), while dense cores in F4 may form with the filaments. In the case of F5, its dynamical property is similar to F8, but it has a shape of a long filament like F4. However, if we focus on the region around F5-C1, small filaments can be seen around the bright hub-like structure by F5-C1 (see the bottom left panel in Figure 10). The peak velocity distribution shown in Figure 6 is similar to that of F8; that is, it has multiple velocity gradients along various directions, although its velocity difference is not as large as that of F8. To confirm that F5 and F5-C1 form via a mechanism similar to F8 and its dense cores, more observations with higher spatial resolution are necessary.

5. Summary and Conclusion

We present dynamical and chemical properties of ~3 pc long filamentary molecular clouds in L1478 in the California MC. We used various molecular lines obtained with the TRAO 14 m antenna: $C^{18}O$(1–0) as a tracer of filaments and N_2H^+(1–0) as a dense core tracer. SO(3_2–2_1) and CS(2–1) molecular lines are observed to investigate the kinematics and chemical evolution of dense cores as well as N_2H^+. We mapped ~1 square degree area in the (1–0) transitions of $C^{18}O$ and ^{13}CO with the noise levels of ~0.1 K[$T_{\rm A}^*$] and the velocity resolution of 0.1 km s^{-1} for both lines. The N_2H^+(1-0) line observations were made over an area of ~480 square arcminute, where $C^{18}O$ is bright, with the noise level of $\lesssim$0.06 K[$T_{\rm A}^*$] and velocity resolution of 0.06 km s^{-1}. SO and CS molecular lines are also observed over an ~440 square arcminute area. The noise level and the velocity resolution are $\lesssim$0.1 K[$T_{\rm A}^*$] and 0.06 km s^{-1}, respectively.

The main results and conclusions are as follows:

1. From this data, 10 filaments are identified with the dendrogram technique. The basic properties of filaments such as length, width, mass, mass per unit length, and mean velocity gradient are derived. We applied the FELLWALKER algorithm to identify dense cores to the N_2H^+ integrated intensity image, and we found eight dense cores in three filaments among the 10 identified filaments.
2. Considering the observed mass per unit length and the effective critical mass per unit length for the filaments, we found that three filaments (F4, F5, and F8) among the 10 filaments are supercritical. These three filaments are found to have dense cores, and YSOs are also reported to

be embedded in F4 and F8. In the supercritical filaments F4, F5, and F8, infall signatures are seen toward the dense cores. From the observational results, we conclude that three supercritical filaments, are gravitationally unstable and continuously contracting.

3. Every filament shows a coherent velocity field. Multiple and grouped velocity components like fibers are frequently found in filaments. Nonthermal velocity dispersions derived with $C^{18}O$ and N_2H^+ indicate that dense cores are subsonic or transonic, while the surrounding gases are transonic or supersonic. However, the distributions of velocity dispersion are found to be different from filament to filament; that is, the nonthermal velocity dispersions of dense cores in F4 are similar to those of the surrounding material, while dense cores in F8 are subsonic or transonic in the transonic or supersonic surrounding filament material. We propose that the formation processes of cores and filaments can be different for their morphologies and environments.

Our forthcoming studies on the physical properties of filaments and dense cores in different star-forming environments will be more helpful to understanding how the filaments and dense cores form.

We appreciate the referee and the editor for the valuable comments and suggestions. We thank J. Montillaud for the valuable discussions and comments. This research was supported by the Basic Science Research Program through the National Research Foundation of Korea (NRF) funded by the Ministry of Education, Science and Technology (NRF-2016R1A2B4012593). M.T. acknowledges partial support from grant AYA2016-79006. P.A.S. recognizes the support by the National Science Foundation through grant #1715867. W.K. was supported by Basic Science Research Program through the National Research Foundation of Korea (NRF-2016R1C1B2013642).

Appendix

We used the astrodendro Python package to identify filaments with the $C^{18}O$ data cube. The first step of the astrodendro algorithm is to make grids of the position–position–velocity space and find local maxima in every grid. We gave initial parameters of four pixels along R.A. × four pixels along decl. × seven pixels along velocity axes for this step. And then structures starting from the local maxima merge the surrounding pixels with lower intensities and become large. When the structures meet a neighboring structure, there are two choices. If the difference between the local maxima and the intensity at the meeting point is larger than the critical value (2σ is used in this step), the structure is identified as an independent structure. But if the difference is less than 2σ, then the local maximum point is rejected and merged into the other structure. There is another parameter to assign the structure as an independent structure: the number of associated pixels. For the structures with an associated number of pixels less than five, we discarded the structures. The merging of structures stops when they meet a neighboring structure or a given minimum intensity (1σ).

Figure 14 shows the tree diagram of Filaments 6, 7, and 8 and sample spectra with their Gaussian fitting results. Panel (a) shows that F6 consists of three leaves (S1, S2, and S3) and two branches (S4 and S5). The leaf S1 includes the local maximum pixel of F6, merges with S2, which is another leaf from the

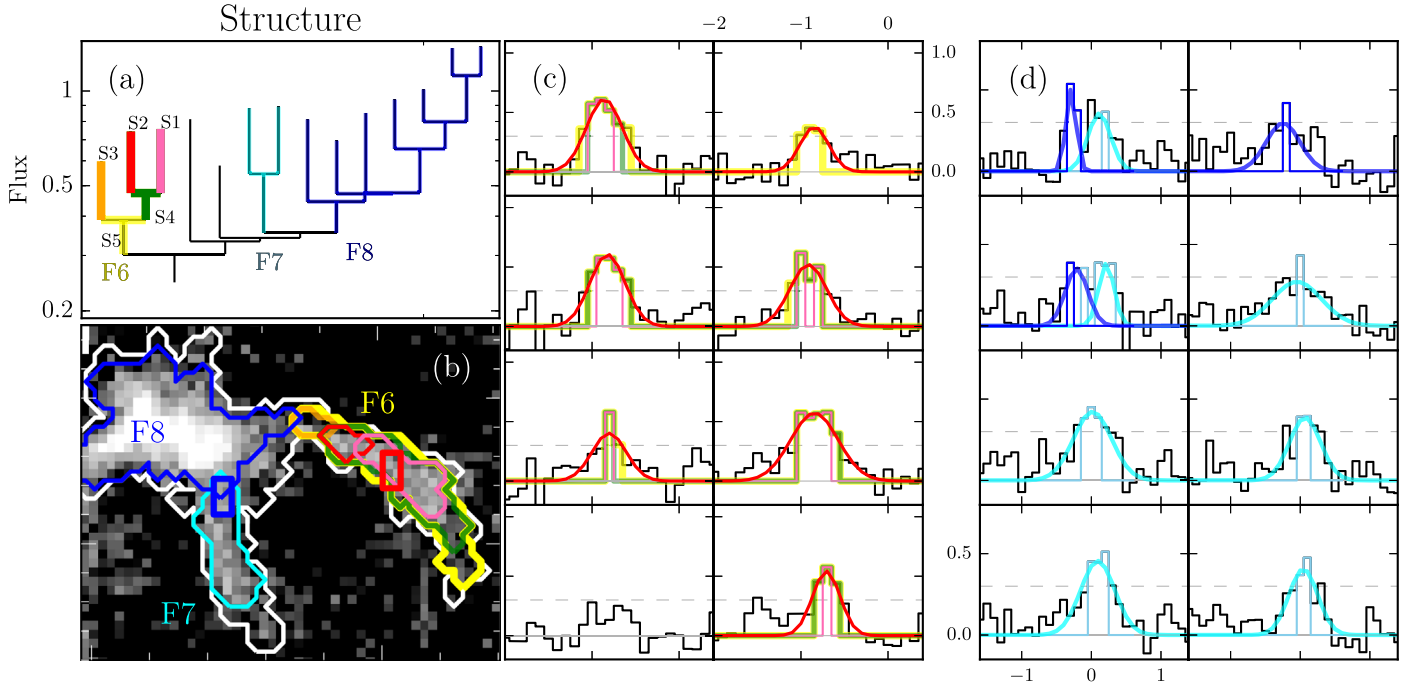

Figure 14. Hierarchical structures of F6, F7, and F8. (a) Tree diagram of F6, F7, and F8. Leaves (that have no substructure, e.g., S1, S2, and S3) and branches (have substructures, e.g., S4 and S5) of F6 are presented with different colors. (b) Contours of leaves and branches derived by the dendrogram technique are overlaid on the $C^{18}O$ moment 0 image to show the spatial distribution of the structures. The same color code as in panel (a) is used, and the grayscale of the integrated intensity map is identical to that of Figure 3. (c) and (d) $C^{18}O$ spectra of the red and blue box regions of panel (b), respectively. The x and y axes are the LSR velocity in km s^{-1} and the antenna temperature in Kelvin, respectively. The observed spectra are given with black histograms, and those of structures (F7, F8, and substructures of F6) are presented with the same color code as in panel (a). The Gaussian fitting results of filaments are overlaid. The dashed line is the 3σ level.

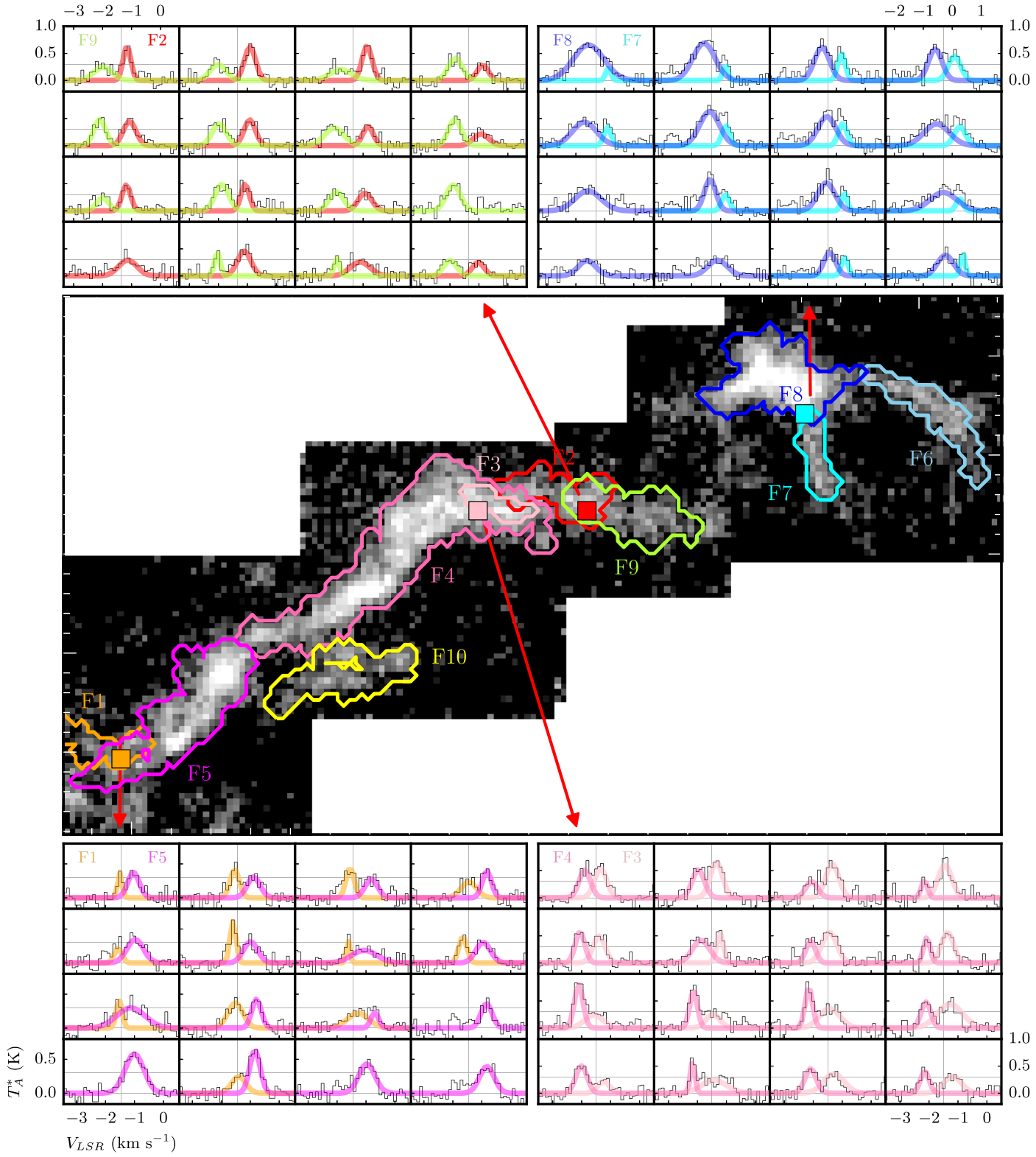

Figure 15. $C^{18}O$ spectra of filaments and the Gaussian fitting results at the areas where filaments are overlapped. Center: filaments overlaid on the $C^{18}O$ integrated intensity map. The squares colored with orange, pink, red, and cyan represent the locations of the spectra shown. Top left: spectra at the red square of the central image where F2 and F9 meet. The *x* and *y* axes of the spectra are the LSR velocity in km s^{-1} and the antenna temperature in Kelvin, respectively. The Gaussian fitting results are plotted with red and green for F2 and F9, respectively. Top right: the same as top left but for F8 and F7 with blue and cyan colors. Bottom left: the same as top left but for F1 and F5 with orange and magenta colors. Bottom right: the same as top left but for F4 and F3 with hot pink and pink colors.

neighboring local maximum, becomes the branch S4, merges again with a leaf S3, and becomes the branch S5. In panels (b) and (c), the spatial and spectral structures of F6 can be seen. Again, the S1 leaf, which has the local maximum pixel (colored with pink), is in the middle of S4 (green) and S5 (yellow), S4 (green contour) encloses S1 (pink) and S2 (red), and S5

(yellow) surrounds S3 (orange) and S4 (green). Likewise, in panel (c), the spectral components of S1 (colored with pink) are surrounded by S4 (green) and S5 (yellow). By checking those components of structures, we confirmed that S5 is a single filament with a coherent velocity structure and named F6.

Panel (d) shows the spectra in the blue box of panel (b), which is the junction of F7 and F8. F7 looks to be connected with F8 in the *Herschel* dust map and the integrated intensity images of ^{13}CO and C^{18}O (see Figure 2). However, double-peak C^{18}O spectra can be seen in the two top left boxes of panel (d), and the lower velocity peak components are connected with northern spectra (F8), and the higher velocity peak components are linked with southern spectra (F7). Hence, F7 is thought to be an independent filament, though its northern part seems to merge with F8 gradually. The blue and cyan histograms are the structures resulting from the dendrogram, and they are identified as independent filaments.

The results shown above confirm that the dendrogram represents well the hierarchical structures of the three-dimensional data. However, the structures (data cube given by dendrogram) do not include whole spectra of the structure as shown with colored histograms in panels (c) and (d) of Figure 14. Hence, we cannot use the data cubes of structures given by the dendrogram but instead carried out Gaussian fitting on C^{18}O spectra to derive the physical properties of filaments, such as the distribution of peak velocity, velocity dispersion, and mass of filaments (Section 3.3). Gaussian fitting is performed automatically with a Python code, and the data cube resulting from the dendrogram is used for its initial guess. Though the data cube from the dendrogram does not fully cover the spectral components, it always contains the peak channel, which can be used as a initial guess of central velocity and velocity dispersion for Gaussian fitting. Hence, we used the velocity of the channel having the maximum intensity at each position and the widths from the data cube resulting from the dendrogram algorithm. The fitting results are overlaid on the spectra in Figure 14. C^{18}O spectra with the Gaussian fitting results at the overlapped positions of filaments are presented in Figure 15. The spectra have clear double-peak components, and each peak is assigned to different structures, indicating that the filaments identified by the dendrogram are distinct structures.

ORCID iDs

Eun Jung Chung https://orcid.org/0000-0003-0014-1527
Chang Won Lee https://orcid.org/0000-0002-3179-6334
Shinyoung Kim https://orcid.org/0000-0001-9333-5608
Gwanjeong Kim https://orcid.org/0000-0003-2011-8172
Paola Caselli https://orcid.org/0000-0003-1481-7911
Mario Tafalla https://orcid.org/0000-0002-2569-1253
Philip C. Myers https://orcid.org/0000-0002-2885-1806
Archana Soam https://orcid.org/0000-0002-6386-2906
Tie Liu https://orcid.org/0000-0002-5286-2564
Kyoung Hee Kim https://orcid.org/0000-0001-9597-7196
Woojin Kwon https://orcid.org/0000-0003-4022-4132
Hyunwoo Kang https://orcid.org/0000-0001-9317-7646

References

André, P., Men'shchikov, A., Bontemps, S., et al. 2010, A&A, 518, L102
Arzoumanian, D., André, P., Didelon, P., et al. 2011, A&A, 529, L6
Arzoumanian, D., André, P., Könyves, V., et al. 2019, A&A, 621, A42
Arzoumanian, D., André, Ph., Peretto, N., & Könyves, V. 2013, A&A, 553, A119
Baug, T., Dewangan, L. K., Ojha, D. K., et al. 2018, ApJ, 852, 119
Berry, D. S. 2015, A&C, 10, 22
Bolatto, A. D., Wolfire, M., & Leroy, A. K. 2013, ARA&A, 51, 207
Broekhoven-Fiene, H., Matthews, B. C., Harvey, P., et al. 2018, ApJ, 852, 73
Broekhoven-Fiene, H., Matthews, B. C., Harvey, P. M., et al. 2014, ApJ, 786, 37
Caselli, P., Myers, P. C., & Thaddeus, P. 1995, ApJL, 455, L77
Caselli, P., Walmsley, C. M., Tafalla, M., Dore, L., & Myers, P. C. 1999, ApJL, 523, L165
Caselli, P., Walmsley, C. M., Zucconi, A., et al. 2002, ApJ, 565, 344
Clarke, S. D., Whitworth, A. P., Spowage, R. L., et al. 2018, MNRAS, 479, 1722
Dame, T. M., Hartmann, D., & Thaddeus, P. 2001, ApJ, 547, 792
Dhabal, A., Mundy, L. G., Rizzo, M. J., Storm, S., & Teuben, P. 2018, ApJ, 853, 169
di Francesco, J., Evans, N. J. I., Caselli, P., et al. 2007, in Protostars and Planets V, ed. B. Reipurth, D. Jewitt, & K. Keil (Tucson, AZ: Univ. Arizona Press), 17
Draine, B. T., & Lee, H. M. 1984, ApJ, 285, 89
Federrath, C. 2016, MNRAS, 457, 375
Frerking, M. A., Langer, W. D., & Wilson, R. W. 1982, ApJ, 262, 590
Garden, R. P., Hayashi, M., Hasegawa, T., Gatley, I., & Kaifu, N. 1991, ApJ, 374, 540
Hacar, A., Kainulainen, J., Tafalla, M., Beuther, H., & Alves, J. 2016, A&A, 587, A97
Hacar, A., & Tafalla, M. 2011, A&A, 533, A34
Hacar, A., Tafalla, M., & Alves, J. 2017, A&A, 606, A123
Hacar, A., Tafalla, M., Forbrich, J., et al. 2018, A&A, 610, A77
Hacar, A., Tafalla, M., Kauffmann, J., & Kovács, A. 2013, A&A, 554, A55
Harvey, P. M., Fallscheer, C., Ginsburg, A., et al. 2013, ApJ, 764, 133
Haugbølle, T., Padoan, P., & Nordlund, Å. 2018, ApJ, 854, 35
Imara, N., Lada, C., Lewis, J., et al. 2017, ApJ, 840, 119
Inutsuka, S.-i., & Miyama, S. M. 1992, ApJ, 388, 392
Inutsuka, S.-i., & Miyama, S. M. 1997, ApJ, 480, 681
Johnstone, D., Rosolowsky, E., Tafalla, M., & Kirk, H. 2010, ApJ, 711, 655
Kauffmann, J., Bertoldi, F., Bourke, T. L., Evans, N. J. I., & Lee, C. W. 2008, A&A, 487, 993
Kirk, H., Johnstone, D., & Tafalla, M. 2007, ApJ, 668, 1042
Kirk, H., Myers, P. C., Bourke, T. L., et al. 2013, ApJ, 766, 115
Kleinmann, S. G., Lysaght, M. G., Pughe, W. L., et al. 1994, ExA, 3, 65
Koch, E. W., & Rosolowsky, E. W. 2015, MNRAS, 452, 3435
Könyves, V., André, P., Men'shchikov, A., et al. 2015, A&A, 584, A91
Lada, C. J., Lombardi, M., & Alves, J. F. 2009, ApJ, 703, 52
Lee, C. W., & Myers, P. C. 2011, ApJ, 734, 60
Lee, C. W., Myers, P. C., & Tafalla, M. 2001, ApJS, 136, 703
Leung, C. M., & Brown, R. L. 1977, ApJL, 214, L73
Liu, T., Li, P. S., Juvela, M., et al. 2018, ApJ, 859, 151
MacLaren, I., Richardson, K. M., & Wolfendale, A. W. 1988, ApJ, 333, 821
Marsh, K. A., Kirk, J. M., André, P., et al. 2016, MNRAS, 459, 342
Maureira, M. J., Arce, H. G., Offner, S. S. R., et al. 2017, ApJ, 849, 89
Müller, H. S. P., Thorwirth, S., Roth, D. A., & Winnewisser, G. 2001, A&A, 370, L49
Myers, P. C. 2009, ApJ, 700, 1609
Ostriker, J. 1964, ApJ, 140, 1056
Padoan, P., Juvela, M., Goodman, A. A., & Nordlund, Å. 2001a, ApJ, 553, 227
Padoan, P., Nordlund, Å., Rögnvaldsson, Ö E., & Goodman, A. 2001b, in ASP Conf. Ser. 243, From Darkness to Light: Origin and Evolution of Young Stellar Clusters (San Francisco, CA: ASP), 279
Palmeirim, P., André, P., Kirk, J., et al. 2013, A&A, 550, A38
Pattle, K., Ward-Thompson, D., Berry, D., et al. 2017, ApJ, 846, 122
Pattle, K., Ward-Thompson, D., Kirk, J. M., et al. 2015, MNRAS, 450, 1094
Peretto, N., Fuller, G. A., André, P., et al. 2014, A&A, 561, A83
Pineda, J. E., Caselli, P., & Goodman, A. A. 2008, ApJ, 679, 481
Pineda, J. L., Goldsmith, P. F., Chapman, N., et al. 2010, ApJ, 721, 686
Punanova, A., Caselli, P., Pineda, J. E., et al. 2018, A&A, 617, A27
Rosolowsky, E. W., Pineda, J. E., Kauffmann, J., & Goodman, A. A. 2008, ApJ, 679, 1338
Sanhueza, P., Jackson, J. M., Foster, J. B., et al. 2012, ApJ, 756, 60
Schnee, S., Enoch, M., Noriega-Crespo, A., et al. 2010, ApJ, 708, 127
Sousbie, T. 2011, MNRAS, 414, 350
Spezzano, S., Bizzocchi, L., Caselli, P., Harju, J., & Brünken, S. 2016, A&A, 592, L11
Tafalla, M., Myers, P. C., Caselli, P., & Walmsley, C. M. 2004, A&A, 416, 191
Tafalla, M., Santiago-García, J., Myers, P. C., et al. 2006, A&A, 455, 577
Wilson, T. L. 1999, RPPh, 62, 143
Xiong, F., Chen, X., Yang, J., et al. 2017, ApJ, 838, 49
Yuan, J., Li, J.-Z., Wu, Y., et al. 2018, ApJ, 852, 12